AGU PUBLICATIONS

JGR

Journal of Geophysical Research: Atmospheres

RESEARCH ARTICLE

10.1002/2017JD026747

Key Points:

- A three-moment microphysics scheme was found to produce the best prediction of a pulse hailstorm and hailfall at surface for an east China case
- Hail prediction verified well against radar-derived maximum estimated hail size (MESH) and available surface observations
- Hail collection of supercooled rain and cloud water dominates the hail production; a three-stage conceptual model for pulse hailstorm life cycle is proposed

Correspondence to:
M. Xue,
mxue@ou.edu

Citation:
Luo, L., M. Xue, K. Zhu, and B. Zhou (2017), Explicit prediction of hail using multimoment microphysics schemes for a hailstorm of 19 March 2014 in eastern China, *J. Geophys. Res. Atmos.*, *122*, 7560–7581, doi:10.1002/2017JD026747.

Received 3 MAR 2017
Accepted 30 JUN 2017
Accepted article online 6 JUL 2017
Published online 27 JUL 2017

Explicit prediction of hail using multimoment microphysics schemes for a hailstorm of 19 March 2014 in eastern China

Liping Luo[1,2], Ming Xue[1,2], Kefeng Zhu[1], and Bowen Zhou[1]

[1]Key Laboratory of Mesoscale Severe Weather/Ministry of Education and School of Atmospheric Sciences, Nanjing University, Nanjing, China, [2]Center for Analysis and Prediction of Storms and School of Meteorology, University of Oklahoma, Norman, Oklahoma, USA

Abstract In the late afternoon of 19 March 2014, a severe hailstorm swept through eastern central Zhejiang province, China. The storm produced golf ball-sized hail, strong winds, and lighting, lasting approximately 1 h over the coastal city of Taizhou. The Advanced Regional Prediction System is used to simulate the hailstorm using different configurations of the Milbrandt-Yau microphysics scheme that predict one, two, or three moments of the hydrometeor particle size distribution. Simulated fields, including accumulated precipitation and maximum estimated hail size (MESH), are verified against rain gauge observations and radar-derived MESH, respectively. For the case of the 19 March 2014 storms, the general evolution is better predicted with multimoment microphysics schemes than with the one-moment scheme; the three-moment scheme produces the best forecast. Predictions from the three-moment scheme qualitatively agree with observations in terms of size and amount of hail reaching the surface. The life cycle of the hailstorm is analyzed, using the most skillful, three-moment forecast. Based upon the tendency of surface hail mass flux, the hailstorm life cycle can be divided into three stages: developing, mature, and dissipating. Microphysical budget analyses are used to examine microphysical processes and characteristics during these three stages. The vertical structures within the storm and their link to environmental shear conditions are discussed; together with the rapid fall of hailstones, these structures and conditions appear to dictate this pulse storm's short life span. Finally, a conceptual model for the life cycle of pulse hailstorms is proposed.

1. Introduction

Hailstorms are a major severe weather hazard in China and many other countries. Severe hail can cause damage such as broken windows, dented cars, damage to crops, and injury to humans and livestock. So far, understanding of the dynamics and microphysics of hailstorms is rather limited. Direct forecasting of surface hail using numerical weather prediction (NWP) models is very challenging; it is necessary to predict accurately both the parent storm and the microphysical processes that occur within it. Further, hail predictability is limited by the rapid development and evolution of hailstorms, the associated rapid growth of forecast errors, uncertainties within microphysics parameterization schemes that are important for hail production, and interactions between microphysics and hailstorm dynamics [*Loftus and Cotton*, 2014].

As reviewed by *Knight and Knight* [2001], hail occurs in many regions of the world. Nonetheless, observational data on hail processes are still highly deficient, and our current understanding of the physics of hailstone growth is still far from complete. *Zhang et al*. [2008] documented the mean annual geographical distribution of hail frequency and seasonal and diurnal variations of hail occurrence in China, with the use of a long record of hail observation data from 1961 to 2005. Important topics, such as the source of hail embryos, the altitude range over which most hail growth occurs, and the tumbling motions of hailstones during hailstorm evolution, remain open questions. The lack of good understanding of hail processes limits our ability to forecast hail, and for fast developing, short-lived, pulse-type hailstorms, producing accurate forecasts and warnings is especially challenging.

Microphysics parameterization schemes within atmospheric models fall into two categories: bulk schemes and spectral bin schemes. In bin schemes, the size distributions or spectral of hydrometeors and cloud condensation nuclei are explicitly predicted using several tens of bins [e.g., *Khain et al*., 2000, 2004; *Lynn et al*., 2005a]. Despite being extremely flexible in terms of particle size distribution (PSD), spectral bin schemes are generally too computationally expensive for most NWP purposes, usually requiring an order of magnitude more computing time than bulk schemes. Moreover, several studies [e.g., *Lynn et al*., 2005b; *Li et al*., 2009; *Khain et al*., 2015] pointed out that various assumptions were also inevitably involved in bin schemes and a wide range of approaches were taken to represent different microphysical processes. For instance, *Khain and Sednev* [1996] assumed immediate melting at the melting level, while in the simulations of *Fan et al*. [2012], melting was calculated by specifying a melting time for ice particles. Uncertainties related to these assumptions will also affect the structure and evolution of simulated precipitation systems.

In bulk schemes, the size spectrum of each hydrometeor category is most commonly defined using a three-parameter gamma distribution function:

$$N(D) = N_0 D^{\alpha} e^{-\lambda D}. \tag{1}$$

In equation (1), the three parametersN_0,α, and λ are the intercept, shape, and slope parameters, respectively. Generally, bulk schemes predict one or two moments (typically the mixing ratio and total number concentration) of the hydrometer particle size distribution (PSD) from which N_0 and $\lambda$are diagnosed (one-moment schemes usually prespecify N_0), while α is specified or diagnosed from the known moments based on empirical relationships. These schemes are known as one- or two-moment schemes, respectively. However, as *Milbrandt and Yau* [2005a, hereafter MY05a] pointed out, the shape parameter can change dramatically during storm evolution and plays a significant role in size sorting and the narrowing of the size spectra of hydrometeor species. By predicting an additional moment, typically the sixth moment or the reflectivity factor, αeffectively becomes prognostic, as is done in the Milbrandt and Yau three-moment scheme [*Milbrandt and Yau*, 2005b, hereafter MY05b]. Simulated hydrometeor fields, precipitation, and storm dynamics are quite sensitive to the choice of the microphysics scheme. Several studies have demonstrated the advantages of multimoment schemes over one-moment scheme [e.g., *Milbrandt and Yau*, 2006a; *Morrison et al*., 2009; *Dawson et al*., 2010, 2015; *Bryan and Morrison*, 2012]. For example, *Dawson et al*. [2010] found that a multimoment scheme produced improved predictions of supercell storm cold pool size and strength, and reflectivity structure, particularly in the forward flank region of the storm. Similarly, in their hailstorm sensitivity experiments, *Milbrandt and Yau* [2006a, 2006b, hereafter MY06a, MY06b] found a dramatic improvement in the prediction of both the hailstorm and the pattern, quantity, and phase of precipitation at the surface when moving from a one-moment to a two-moment scheme, and even better performance in terms of hail prediction when moving to a three-moment scheme. More recently, *García-Ortega et al*. [2017] examined the performance of multiphysics ensembles in convection precipitation forecast on hail days in northeastern Spain and concluded that the performance of the Morrison two-moment scheme was better than other one-moment schemes.

In the past few decades, various efforts have been made to improve hail forecasts [e.g., *Moore and Pino*, 1990; *Brimelow et al*., 2002; *Brimelow and Reuter*, 2009; *García-Ortega et al*., 2012; *Gagne et al*., 2014; *Adams-Selin and Ziegler*, 2016; MY06a], the ability to explicitly forecast hailfall at the surface is still limited. Since more advanced multimoment microphysics schemes have the capability to predict hail size distribution, explicit hail predictions are being attempted using NWP models with real cases. MY06b represents one of few attempts to produce explicit predictions of hail (for a hailstorm in Canada) using a storm-scale NWP model, while *Snook et al*. [2016] is another more recent examples for hail prediction over the United States central Great Plains. More studies are needed, particularly for different types of storms and for storms from different regions of the world.

In this study, we perform a numerical study on a pulse-type severe hailstorm that occurred on 19 March 2014, in Taizhou City, Zhejiang province, China. The storm produced walnut-sized hail at ground level, as well as strong winds and lightning. As pointed out by *Burgess and Lemon* [1990], pulse-type storms typically develop in environments with strong instability and weak vertical wind shear. Such storms can have strong updrafts and produce severe weather, including large hail and damaging winds. *Cerniglia and Snyder* [2002] examined many parameters of severe pulse storms, focusing on producing warnings for such storms in the northeastern United States. They found that the most useful warning criteria for this type of storm are elevated average height of maximum echo top for 45, 50, 55, 60, and 65 dB*Z* reflectivity thresholds, high values of vertically integrated liquid, and high probability of severe hail. However, few modeling studies of pulse hailstorms have been performed, especially using real data. Detailed knowledge of the evolution of microphysical processes during the storm's lifecycle is also lacking.

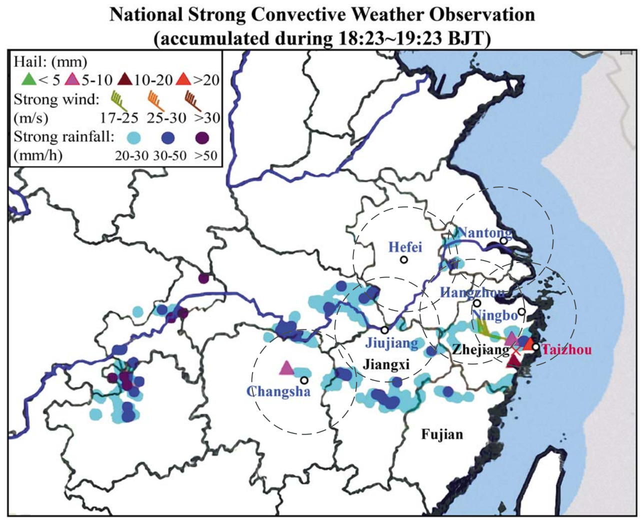

Figure 1. Twenty-four hour reports of severe weather in eastern China, starting from 1500 UTC 18 March 2014. The Taizhou City on the coast where hail was reported is labeled. The Yangtze River through the middle of the map is drawn in blue. Also shown are the province borders. The locations marked by open black circles indicate the six operational S-band radars at Nantong, Hefei, Hangzhou, Jiujiang, Changsha, and Ningbo. The large dashed gray circles denote the 230 km range rings for the radars. The red cross denotes the location of the extracted sounding shown in Figure 3. Provinces are labeled in black, and the city of Taizhou is labeled in red (Obtained from Severe Weather Report Maps of Chinese Meteorology Society).

The purposes of this study are twofold. First, the ability of a storm-scale NWP model to explicitly predict hail for the 2014 Taizhou City pulse hailstorm using bulk microphysics schemes that predict different number of hydrometeor moments will be evaluated. Second, based on the CNTL simulation using the three-moment MY scheme (which predicts the most consistent surface hail size distribution with observations), the dominant microphysical processes responsible for the hail production will be investigated and the structure and evolution of the hailstorm during its short lifespan will be documented. The Advanced Regional Prediction System (ARPS) [*Xue et al.*, 2000, 2001] with one-, two-, and three-moment Milbrandt and Yau (hereafter MY) microphysics schemes is used, and the performances of hail prediction using these schemes are compared.

This paper is organized as follows: in section 2, a brief overview of the 19 March 2014 hailstorm case is given. The ARPS model setup and verification metrics used for hail prediction are documented in sections 3 and 4, respectively. In section 5, hail forecasts produced using different microphysics schemes are verified. In section 6, we further discuss the dynamical and microphysical characteristics during different stages of the hailstorm life cycle, particularly the microphysical characteristics associated with the growth and decay of the hailstorm. Microphysical budget analyses are presented in this section to identify the dominant processes of hail growth. In section 7, a conceptual model is proposed for pulse-type hailstorms, along with a general summary and proposed topics for future research.

2. Case Overview

During spring-to-summer transition, with the gradual onset of the East Asian summer monsoon [*Ding*, 1994], cold dry air from the north interacts with warm moist air from the south in the Yangtze River Basin region in China, subjecting the region to high likelihood of severe convective weather. A hailstorm occurred during such a transition season on 19 March 2014 near the city of Taizhou on the eastern coast of China's Zhejiang province (Figure 1). The hailstorm was observed by multiple operational S-band Doppler radars, including those at Nantong, Hefei, Hangzhou, Jiujiang, Changsha, and Ningbo (Figure 1). On that day, a cold front moved southeastward and swept across the middle and lower reaches of the Yangtze River Basin. As the front moved into Zhejiang province, a series of convective storms initiated. One of the storms was initiated at around 0850 UTC and produced a large amount of hail while passing over Taizhou City at approximately 0930 UTC. The hailstorm lasted about an hour and produced a large number of walnut-sized hailstones, completely covering the ground within about half an hour. The maximum registered hail size was 33 mm. Intense lighting and damaging winds (>17 m s^{-1}) were also reported with these storms.

The synoptic-scale environment associated with the event is presented in Figure 2. At 0600 UTC on 19 March 2014, the East Asian coast region was experiencing a strong, northeastward tilted, semipermanent East Asian trough (EAT) at upper levels (Figures 2a and 2b), and an East Asian upper tropospheric jet stream (EAJS). The jet axis was located at about 32°N and to the east of 120°E, with a maximum wind speed exceeding 50 m s^{-1}

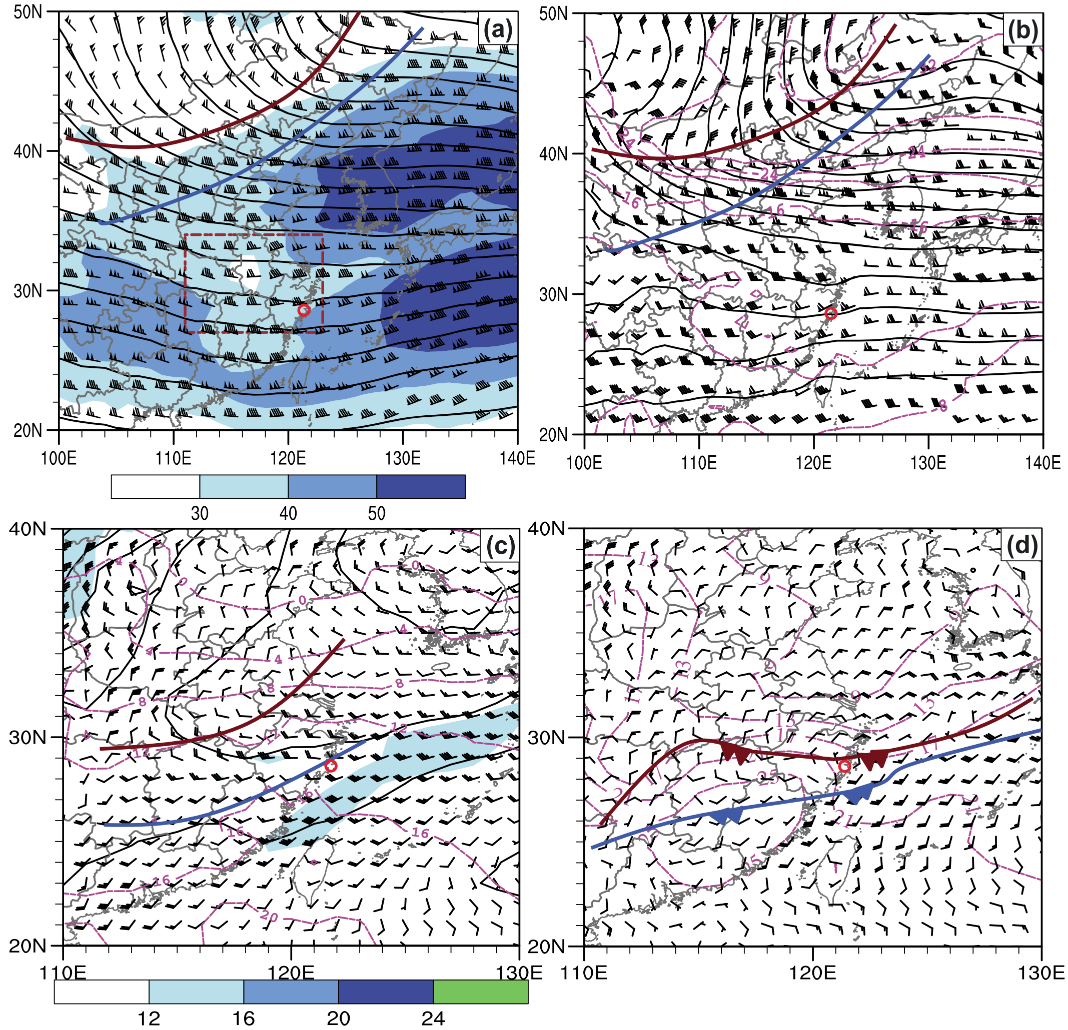

Figure 2. Synoptic features of (a) 200 hPa, (b) 500 hPa, (c) 850 hPa, and (d) 1000 hPa at 0600 UTC 19 March 2014, showing wind barbs (one full barb denotes 2.5 m s^{-1}), wind speed (shaded, m s^{-1}), temperature (red dashed contours, with interval of 4°C), and geopotential height (solid gray contours, geopotential meters). The bold solid lines in Figures 2a and 2b, 2c, and 2d indicate trough lines, shear line, and the cold front, respectively, at 0600 UTC (brown) and 1200 UTC (blue). Taizhou City is indicated by the red circle in each panel.

(Figure 2a). The Yangtze River Basin region (as shown by the brown dashed box in Figure 2a) was located in the region ahead of the EAT and the right-rear entrance of the EAJS, where favorable positive vorticity advection forcing from the EAT existed aloft, and concurrent upper level divergence acted to enhance the upward vertical motion. Moreover, strong midlevel cold air advection from the north was superimposed on low-level warm advection from the south in this region, resulting in destabilization of the atmosphere (Figures 2b and 2c). At 1000 hPa (Figure 2d), there is strong wind convergence along the cold front. From 0600 to 1200 UTC, the cold front and wind shear line at the low levels traversed much of Zhejiang province, resulting in multiple reports of severe weather along the way (Figures 2c and 2d).

Because of the lack of observed soundings close to the time of hailstorm initiation, a sounding is extracted from the National Centers for Environmental Prediction (NCEP) 1°×1° FNL analysis data at (28°N, 120°E), a location roughly 30 km southwest of Taizhou City denoted by a red cross in Figure 1, at 0600 UTC—approximately 2 h before the storm is detected by the Taizhou radar. In this sounding (Figure 3), relatively cool air is present between 400 and 650 hPa, contributing to convective available potential energy (CAPE) of about 1900 J kg^{-1}, with convective inhibition of 43 J kg^{-1}; these conditions are conducive for deep convection, particularly in the presence of forcing from low-level convergence. Horizontal winds veer rapidly with

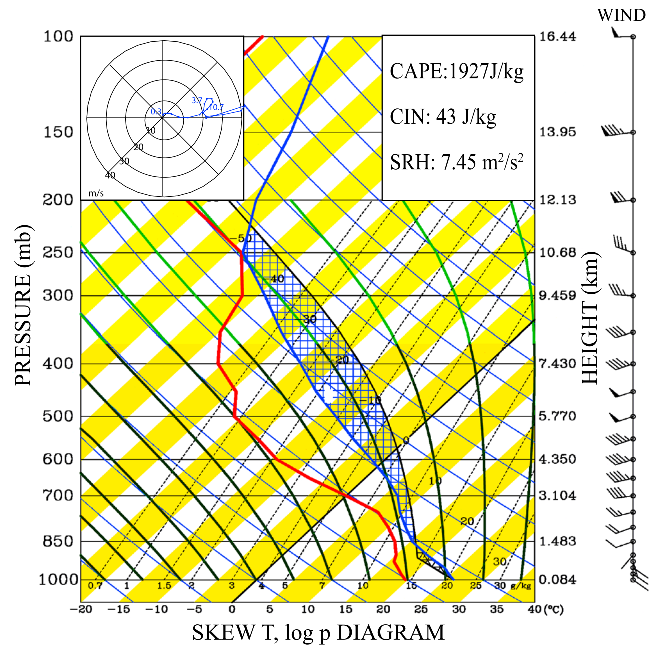

Figure 3. Skew *T* plot of a sounding extracted from NCEP FNL analysis data at (28°N, 120°E) at 0600 UTC 19 March 2014 near Taizhou.

height from southeasterly at the surface to westerly at the 850 hPa level and above. At 850 hPa, the wind speed is only about 5 m s^{-1}, but it increases to more than 25 m s^{-1} at 500 hPa and above. This moderate, unidirectional vertical wind shear causes the storm-relative helicity (SRH) between 0 and 3 km to remain very low (7.45 m^2 s^{-2}). An environment with moderate wind shear, relatively high CAPE, and low SRH generally favors short-lived, nonsupercell, pulse-type storms [*Burgess and Lemon*, 1990]. Moreover, a layer of high humidity was present in the sounding below 700 hPa, making the atmosphere conducive to convective initiation, particularly given the low-level convergence forcing associated with the cold front. Between 700 and 400 hPa, the atmosphere is relatively dry, likely due to the midlevel advection of cold, dry air from the north. Studies [e.g., *Costa et al.*, 2001; *Webb and Muirhead*, 2002; *Craven et al.*, 2004] have shown the importance of a dry layer over a warm moist layer close to the ground to be favorable for larger hail at the ground, due to reduced melting of hailstones as they fall. In summary, the environment during this case was favorable for intense but short-lived pulse-type hailstorms.

3. Experiment Setup

The Taizhou hailstorm case is simulated using the ARPS model [*Xue et al.*, 2000, 2001, 2003]. ARPS is a three-dimensional, nonhydrostatic compressible NWP model that uses generalized terrain-following coordinates. All simulations in this study are initialized at 1200 UTC on 18 March 2014 and run for 30 h, ending at 0000 UTC on 20 March 2014. Initial conditions, and boundary conditions at 6 h intervals, are obtained from the NCEP Global Forecast System real-time analyses at 0.5°×0.5° resolution.

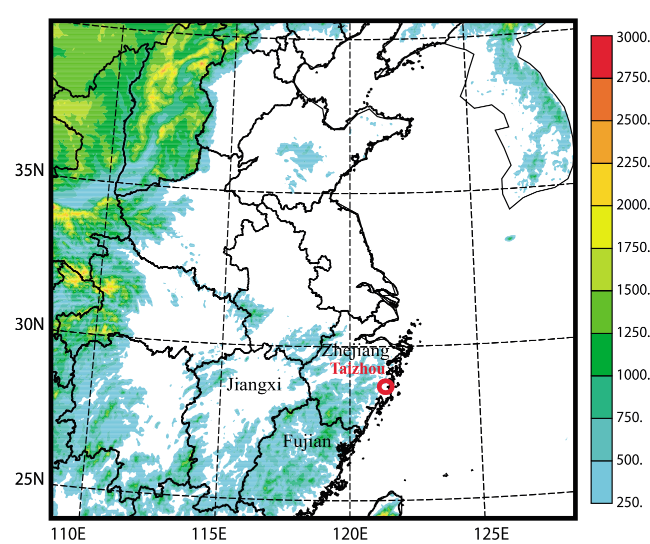

Figure 4. Model domain of the 19 March 2014 Taizhou hailstorm simulations. Terrain elevation (m) is plotted in color. Taizhou City is marked by a red circle, and nearby provinces are labeled in black.

The model domain (Figure 4) covers a 1980 × 1800 km^2 region using 661 × 601 grid points, centered at (32.5°N, 118.5°E), and the horizontal grid spacing is 3 km. The vertical resolution changes from 50 m near the ground to about 1000 m at the model top that is located at about 25 km above mean sea level with an average spacing of 500 m, and the vertical grid stretching uses a hyperbolic tangent function as described in *Xue et al.* [1995]. Fifty three vertical layers are used, with about 18 layers located below 2 km above ground level. Subgrid-scale turbulent mixing is calculated using a 1.5-order

Table 1. List of 3 km Sensitivity Experiments

Run	Description
CNTL	Three-moment; full version of scheme
DiagA	Two moment; diagnostic of relation for $\alpha_x = f(D_{mx})$ $x \in (r, i, s, g, h)$
FixA0	Two moment; fixed $\alpha_x = 0$
FixA1	Two moment; diagnosis of experiment CNTL; $\alpha_{\rm rain} = 2$, $\alpha_{\rm hail} = 1$, $\alpha_{\rm ice/snow/graupel} = 0$
Single	One-moment; $\alpha_x = 0$; $Nt\text{cloud} = 1\times10^8 m^{-3}$; $N_{0r} = 8\times10^6 \mathrm{m}^{-4}$, $N_{0s} = 3\times10^6 \mathrm{m}^{-4}$, $N_{0g} = 4\times10^5 \mathrm{m}^{-4}$, $N_{0h} = 4\times10^4 \mathrm{m}^{-4}$

turbulence kinetic energy (TKE) scheme, while vertical turbulence mixing within the unstable convective boundary layer is parameterized using a different 1.5-order TKE scheme, based on *Sun and Chang* [1986]. The *Zalesaka* [1979] multidimensional flux-corrected transport scheme is applied to potential temperature, water variables, and TKE, while fourth-order discretization is used for pressure and momentum advection. The upper and lower boundaries are set as rigid walls with zero wall-normal velocity, surface fluxes are computed using stability-dependent drag formulations, and a Rayleigh damping layer is applied above 12 km. More details on the ARPS physics options can be found in *Xue et al*. [2001, 2003]. We realize that the 3 km grid spacing is relative large for hailstorm simulations. For another eastern China hailstorm case that we are working on, we found qualitatively similar results between 3 km and 1 km simulations, suggesting that the 3 km results presented in this paper should be at least qualitatively valid.

Microphysics processes are clearly very important for hail prediction. In this study, we performed several simulations, using one-, two-, and three-moment versions of the MY microphysics scheme (MY05a and MY05b). The MY microphysics schemes contain six distinct hydrometeor categories: cloud water, rain water, cloud ice, snow, graupel, and hail. The graupel category further includes moderate-density graupel formed from heavily rimed ice or snow. The hail category includes high-density hail converted from graupel and frozen raindrops. Each hydrometeor species is represented by a gamma distribution.

The three-moment MY scheme is used in the control experiment CNTL; the scheme predicts three moments for all precipitating hydrometeor categories, including rain, ice, snow, graupel, and hail. Four other experiments use variants of lower moment MY schemes. A summary of the key parameters of the MY scheme variants used in the simulations is present in Table 1. Three of the simulations, named FixA0, FixA1, and DiagA, apply variants of the MY two-moment scheme with different assumed shape parameters (α). FixA0 sets α to a default constant value of 0 for all hydrometeor categories while FixA1 uses a fixed α value of 2 for rain, 1 for hail, and 0 for other categories. The α values for rain and hail in FixA1 are approximate values of α in the small domain (denoted by the red dashed box in Figure 5d) over the simulated hailstorm from experiment CNTL. In DiagA, α is diagnosed from the mean mass diameter of the corresponding categories, as given by equations (12) and (13) of MY05a for hail and other hydrometeors, respectively. The MY one-moment scheme was also tested in the simulation named Single. Within a one-moment scheme, both intercept and shape parameters for all categories are fixed to prespecified default values as presented in Table 1 (which may not be appropriate for particular storms), while in the three-moment MY scheme, the intercept, shape, and slope parameters of the gamma distributions of all the categories are predicted, effectively, providing more freedom and potential for the model to predict a more accurate hail PSD.

4. Evaluation Metrics for Hail Prediction

4.1. Maximum Estimated Size of Hail

Owing to the lack of in situ observations and frequent substantial biases in hail reports (due to population distribution, etc.), radar observations with high spatiotemporal resolutions tend to be the best available data sets to verify hail forecasts [*Snook et al*., 2016]. Here we consider the radar-based maximum estimated size of hail (MESH) algorithm [*Witt et al*., 1998] to estimate the maximum expected hail size. This algorithm assumes that high reflectivity (Z), where reflectivity >40 dBZ above the 0°C level is a likely indicator of hail and assigns a higher probability of hail (i.e., a larger weight in the algorithm) to the presence of very high reflectivity (reflectivity >50 dBZ) above the −20°C level. This algorithm has proven to be a useful indicator of overall hail damage potential operationally. Following *Snook et al*. [2016], reflectivity data sets from multiple radars are interpolated to the model grid to derive the radar-based MESH. The MESH values of the sensitivity runs are

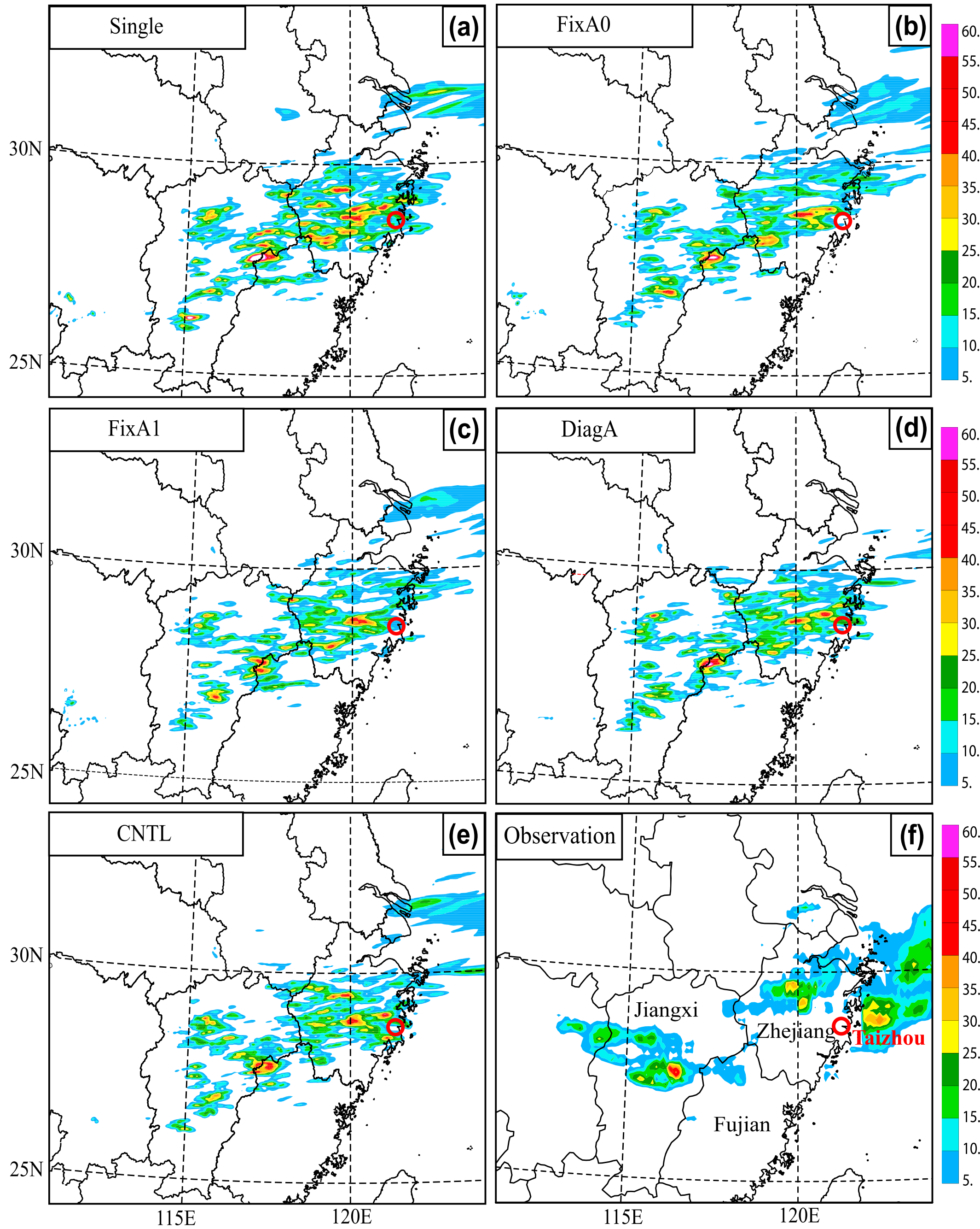

Figure 5. Six hour surface accumulated precipitation (mm) from 0600 to 1200 UTC on 19 March 2014 from experiments (a) Single, (b) FixA0, (c) FixA1, (d) DiagA, (e) CNTL experiments, and (f) observation from improved merged precipitation product. Taizhou City is marked by a red circle, and Zhejiang, Jiangxi, and Fujian provinces are labeled in black in Figure 5f. The red dashed box in Figure 5f denotes the domain of Figure 6.

derived from the model reflectivity output using various microphysics schemes. Below are equations in the MESH algorithm [*Witt et al.*, 1998]:

$$E\cdot = 5\times10^{-6}\times10^{0.084Z}\times W(Z) \tag{2}$$

$$\mathrm{SHI} = 0.1\int_{H_0}^{H_T} W_T(H)\,E\cdot \mathrm{d}H \tag{3}$$

$$\mathrm{MESH} = 2.54(\mathrm{SHI})^{0.5} \tag{4}$$

where

$$W(Z) = \begin{cases} 0 & \text{for } Z \leq Z_L \\ \dfrac{Z - Z_L}{Z_U - Z_L} & \text{for } Z_L < Z < Z_U \\ 1 & \text{for } Z \geq Z_U \end{cases} \tag{5}$$

$$W_T(H) = \begin{cases} 0 & \text{for } H \leq H_0 \\ \dfrac{H - H_0}{H_{m20} - H_0} & \text{for } H_0 < H < H_{m20} \\ 1 & \text{for } H \geq H_{m20} \end{cases} \tag{6}$$

In equation (2), radar reflectivity Z is transformed into the flux of hail kinetic energy $\dot{E}$ through a weighting function $W(Z)$that defines the transition zone between rain and hail. Here we set the values of upper and low reflectivity limits $Z_U$and Z_L in $W(Z)$ (see equation (5)) to be 40 and 50 dBZ. Severe hail index (SHI) is defined in equation (3), where $W_T(H)$ is a temperature-based weighting function given in equation (6), H, H_0, H_T, and $H_{m20}$are the height levels of the ARPS model domain, the melting level, the top of the storm cell and the −20°C environmental temperature, respectively. Following *Snook et al*. [2016], due to the lack of direct temperature observations, the predicted temperature of experiment CNTL is used in the calculation of the radar-based MESH. Equation (4) gives MESH (in millimeters).

4.2. Cumulative Number Concentration of Hailstone

Another way of assessing the hail size prediction is to calculate the total number concentration of hailstones larger than a given threshold per cubic meter within the hailstorm. This is given by$N_{Dh}(D)$, the total number concentration of hailstones larger than diameter D (MY06a):

$$N_{Dh}(D) = \int_D^\infty N_h(D^*)\mathrm{d}D^*, \tag{7}$$

where the size distribution of hail

$$N_h(D) = N_{0h} D^\alpha e^{-\lambda D} \tag{8}$$

is described by a three-parameter gamma distribution function.$N_{Dh}(D)$in equation (7) is the cumulative density function of the total number of hailstones with diameter larger than D and can be used to examine the instantaneous number of large hailstones aloft. Here we set a threshold value of 10^{-3} m^{-3} for physical existence of hailstones, following MY06a.

5. Simulation Results and Verification

In this section, the results of model simulations of the hailstorm are presented. To evaluate how well the hailstorm is simulated by the model in general, the predicted surface accumulated precipitation is compared with an improved gauge-satellite-merged hourly precipitation data set at a 0.1° × 0.1° resolution covering continental China. This precipitation product was generated using hourly rain gauge data from more than 30,000 automatic weather stations in China and the Climate Precipitation Center Morphing (CMORPH) precipitation product [*Joyce et al*., 2004] via the improved probability density function and optimal interpolation (PDF-OI) technique. Assessments by *Shen et al*. [2014] indicate that the PDF-OI technique used effectively reduces systematic bias and random errors compared with the original CMORPH precipitation. In addition, hail predictions are evaluated by comparing model simulated and radar-derived MESH fields. Model-predicted reflectivity fields are also compared to radar observations. Comparisons of microphysical-related fields are presented and discussed in section 6.

5.1. Accumulated Surface Precipitation

The 6 h surface accumulated precipitation fields from 0600 to 1200 UTC in the simulations are compared against the improved merged precipitation product over China as aforementioned (Figure 5). Observed precipitation extends from the northwest corner of Fujian province into southwest Zhejiang province and through the eastern coastal region of Zhejiang province. Within Jiangxi province west of Zhejiang, the observed precipitation pattern shows a southeast northwest orientation (Figure 5f). However, for experiment Single using the one-moment scheme, the rainfall amount is highly overestimated, especially in the middle part of Zhejiang province where a large area with heavy precipitation exceeding 40 mm is predicted (Figure 5a). The overall patterns of predicted rainfall of other sensitivity runs using multimoment microphysics schemes are relatively similar to that of observed rainfall, although there are intensity differences. Model simulations (Figures 5b–5e) show four to six small areas of high precipitation amounts exceeding 40 mm within the general precipitation regions, and two areas of observed high rainfall in northwest of Zhejiang province (Figure 5f) are well captured, although the observed rainfall maximum is between 35 and 40 mm. The rainfall maximum in southeast Jiangxi province shows the best agreement between the observation and model simulations. The differences in the maximum amounts and their distributions can be partly attributed to the lower resolution of rain gauge network compared to the grid spacing of the model. It should also be noted that the model-simulated precipitation includes hail mass, while the rain gauge measurements most likely underestimate the hail contribution to precipitation.

The above comparisons suggest that the precipitation system is captured reasonably well within Zhejiang province, although there are significant differences in small-scale details. The southeast northwest orientated precipitation pattern within Jiangxi province appears to be captured best in experiment CNTL (Figure 5e). The general characteristics of precipitation among the four simulations using multimoment schemes (Figures 5b–5e) are much more similar to one another than to the observation. Some spurious precipitation southwest of the main precipitation band is present in all experiments.

5.2. Comparison of Model Simulated and Radar-Based MESH

Swaths of MESH derived from gridded radar data and the simulations between 0940 and 1120 UTC at 5 min intervals are presented in Figure 6. There is one primary MESH swath in the observed MESH field (Figure 6f), corresponding to the hailstorm over Taizhou, with a maximum value of about 35 to 40 mm. Over the Taizhou City, a maximum hail size of 33 mm was registered. Compared to the observations, the forecast MESH swaths in Single, FixA0, FixA1, and DiagA (Figures 6a–6d) have scattered cores of lower MESH values, except for experiment CNTL (Figure 6e) which exhibits two cores of MESH values reaching 40 mm, although their locations are about 60 km to the west-northwest of Taizhou. These two cores correspond to those two east-west oriented precipitation cores found in Figure 5e. The displacement of the MESH core is at least partially due to overly slow southward movement of the simulated storms.

Among the MESH swaths produced by the simulations, those of FixA0 are closest to those of CNTL, although FixA0's maximum values stay below 25 mm (Figure 6b). Even though the fixed values of α in FixA1 are based on three-moment CNTL simulation, the differences in simulated MESH between FixA1 and CNTL are significant. The storms' evolution within the experiments using two-moment schemes suggests that the smaller MESH values derived from the two-moment schemes appear to be a result of more rapid dissipation of the simulated storms (not shown), since in such cases the hailstones have less time to grow. This suggests the α approximation is not enough to predict the hydrometeor size distributions accurately; in reality, αcan exhibit significant spatial and temporal variation throughout the storm. Nonetheless, in DiagA, where α is diagnosed as a function of the mean mass diameter of the corresponding categories, the MESH prediction is not noticeably improved. As indicated in MY05a, the two-moment MY scheme with diagnosed α still displays a significant discrepancy in simulation results from that of the three-moment scheme.

Moreover, the radar reflectivity of the one- and two-moment MY schemes is diagnosed from the mass content and total number concentration, as given by equation (6) in MY05a. While for the three-moment scheme, the radar reflectivity factor is predicted, not diagnosed as in the one- or two-moment schemes. The prediction of reflectivity makes α effectively prognostic, which plays a significant role in determining the rate of size sorting and instantaneous growth rates related to the moments (MY05a). Above all, MESH prediction using the full three-moment MY scheme in CNTL best matches observations, predicting a maximum hailstone size of about 40 mm in an east-west oriented swath (Figure 6e).

We note here that the original MESH algorithm of *Witt et al*. [1998] was developed for estimating hail size larger than 19 mm only. Values below 19 mm found in Figure 6 should be viewed with major caution. We choose to include these values so that some indication of possible hailfall can still be seen for experiments FixA1 and DiagA, whose values are all below 20 mm.

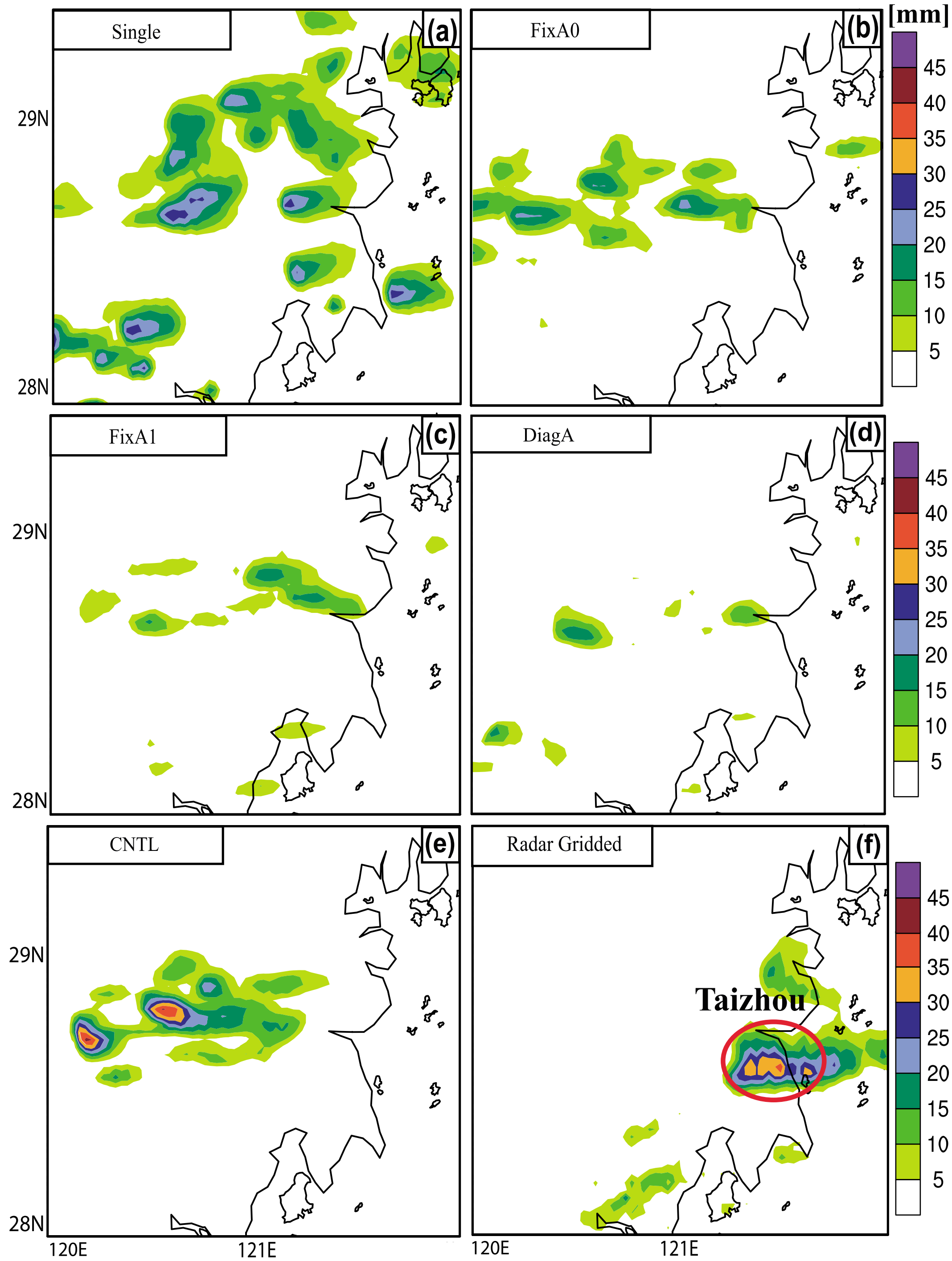

Figure 6. Simulated MESH with one-, two- and three-moment microphysics schemes, namely (a) Single, (b) FixA0, (c) FixA1, (d) DiagA, (e) CNTL, and (f) observed swaths of MESH derived from WSR-98D radar observations. The MESH fields are created as a composite from observed/simulated data between 0940 and 1120 UTC at 5 min intervals.

6. Simulated Reflectivity and Microphysical Fields in CNTL

6.1. Simulated Reflectivity Fields in CNTL

Given that experiment CNTL, which uses the three-moment microphysics scheme, produces the best MESH swath compared to radar-derived MESH, we will focus on examining CNTL in greater detail in this section.

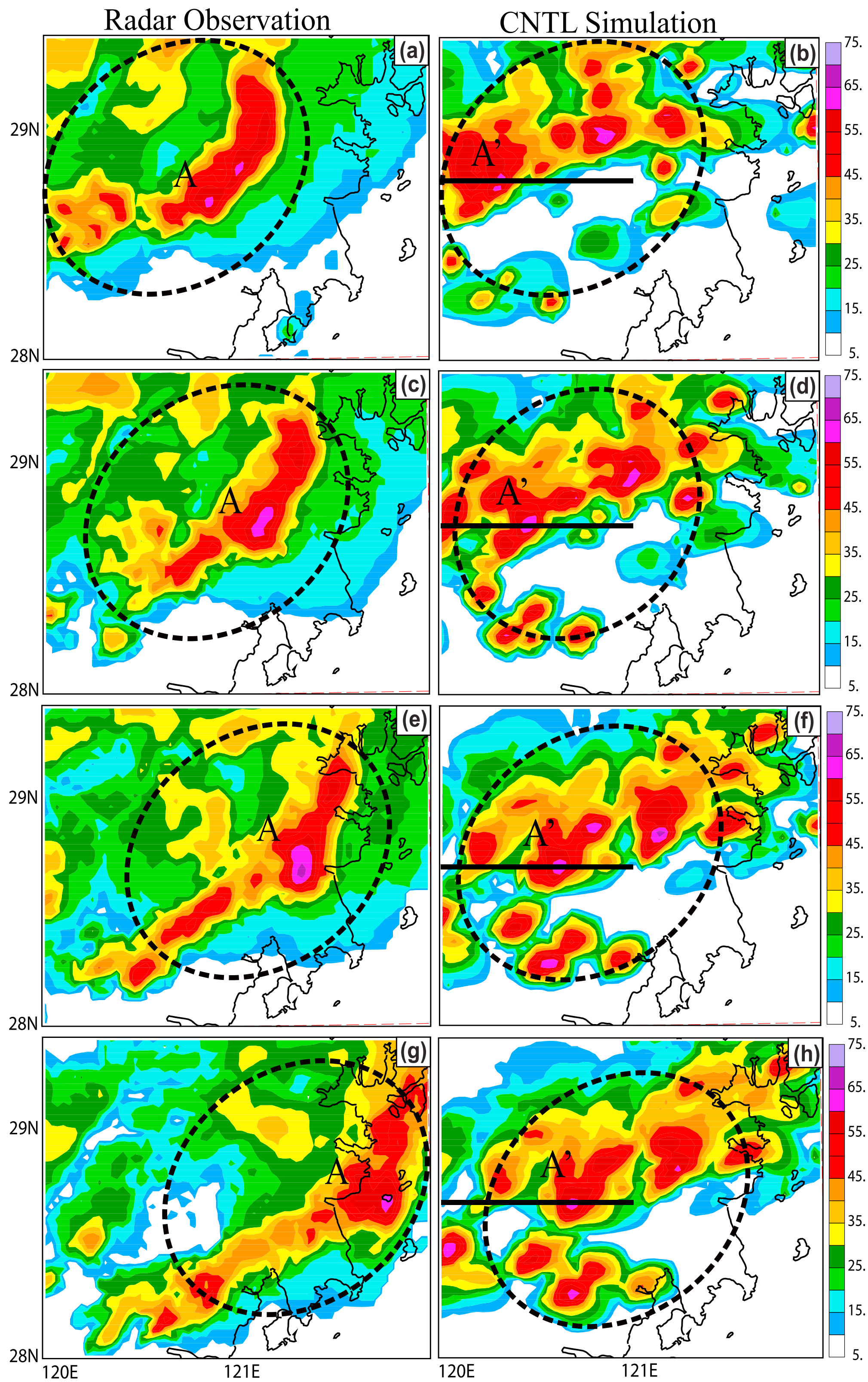

Figure 7. Composite (column-maximum) reflectivity fields from (a, c, e, and g) operational radars and (b, d, f, and h) CNTL simulation. The radar fields are from 0850 to 0950 UTC at 20 min intervals, while the simulated fields are from 0940 (Figure 7b), 1000 (Figure 7d), 1030 (Figure 7f), and 1100 UTC (Figure 7h), taking into account of timing errors of the simulations compared to the observations.

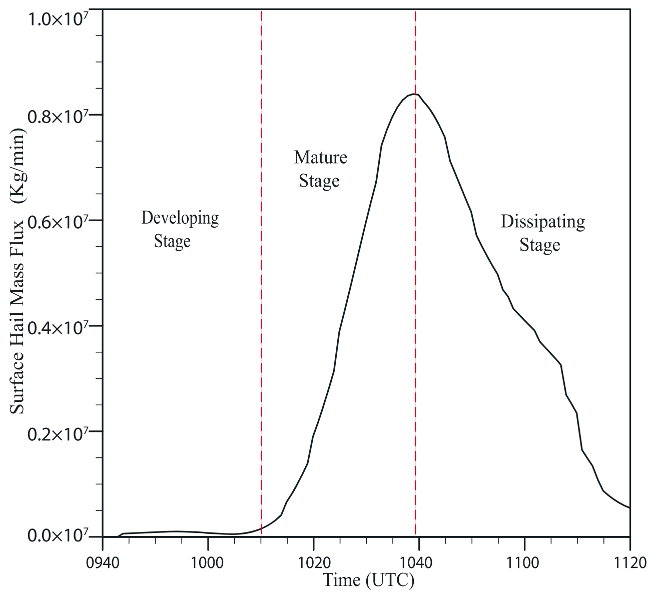

Figure 8. Time series for domain total surface hail mass flux during the short lifespan of hailstorm, characterized by three stages, the developing stage, from 0940 to 1010 UTC, the mature stage, from 1010 to 1040 UTC, and the dissipating stage from 1040 UTC onward.

Simulated composite (column maximum) reflectivity from CNTL, at 0940, 1000, 1030, and 1100 UTC is compared to observed composite reflectivity at 0850, 0910, 0930, and 0950 UTC in Figure 7. The time lag in the comparison is applied to compensate for the timing delay in the simulated storms and the relatively slow southward movement of the storms in the simulation. At the times shown, the simulation presents close to the best match with observations. In other words, the simulated storms are delayed by approximately 1 h compared to observations. While the simulated reflectivity appears more scattered than the observations, the strongest reflectivity core of simulated storm A′ in CNTL can be considered the counterpart of observed storm A (Figure 7). In the radar observations, storm A is the strongest, producing reflectivity of up to 75 dB*Z*. Such high values of reflectivity are observed only in hail-producing storms; storm A is responsible for most of the hailfall over Taizhou (as well as the corresponding MESH swath in Figure 6f). In the simulation, storm A′ is responsible for the main swath of high MESH values (Figure 6e). Storm A′ is therefore considered the counterpart of observed storm A and is analyzed in detail below.

6.2. Simulated Microphysical Fields in CNTL

Most existing studies on hailstorms have been based on either observations or idealized laboratory or numerical experiments [e.g., *Cheng and English*, 1982; *Heymsfield*, 1982; *Guo and Huang*, 2002; *Kennedy et al.*, 2014; *Fernández-González et al.*, 2016]; relatively few studies compare simulated microphysical fields to observed hail events. Given the reasonable resemblance of the model-predicted MESH and reflectivity fields for the Taizhou hailstorms to radar observations, we will further examine hail-related microphysical fields and rain PSDs during different stages of the hailstorm development. To investigate the dominant processes responsible for hailstone growth, we perform a microphysical budget analysis based on the equation of tendency for hail mass mixing ratio, as given by equation (A7) of MY05b. Specifically, the three predicted moments, namely, the sixth moment reflectivity (Z), third-moment mass content (q) and zeroth moment total number concentration (N_t), and the derived mass-weighted mean diameter (D_m) for hail, are examined during the storm evolution. Since the microphysical processes of rain and hail have close interactions, the behaviors of the rain PSD are also discussed.

To characterize the time evolution of the hailstorm, hail mass flux at the surface is calculated and used to define different stages of the simulated hailstorm. Time series of the surface hail mass flux integrated over the domain of Figure 7 are presented in Figure 8. The flux here is defined to be the total hail mass arriving at the surface of the domain per minute. This procedure helps identify three distinct stages in the storm's lifetime: a developing stage between 0940 and 1010 UTC; a mature stage between 1010 and 1040 UTC, and a dissipating stage from 1040 UTC onward. During the developing stage of the storm, hail has not fallen to the ground; the surface hail flux is nearly zero. In the mature stage, the hail flux increases rapidly, reaching a maximum value of about 0.8×10^7 kg min^{-1} within about 30 min at 1040 UTC. After 1040 UTC, the surface hail flux decreases sharply, corresponding to the rapid collapse of the hailstorm. In the early part of this dissipating stage, hailfall at the surface remains substantial. After 40 min (1120 UTC), hailfall ceases. Overall, the period with intense hailfall lasts approximately 1 h, typical of a pulse-type storm.

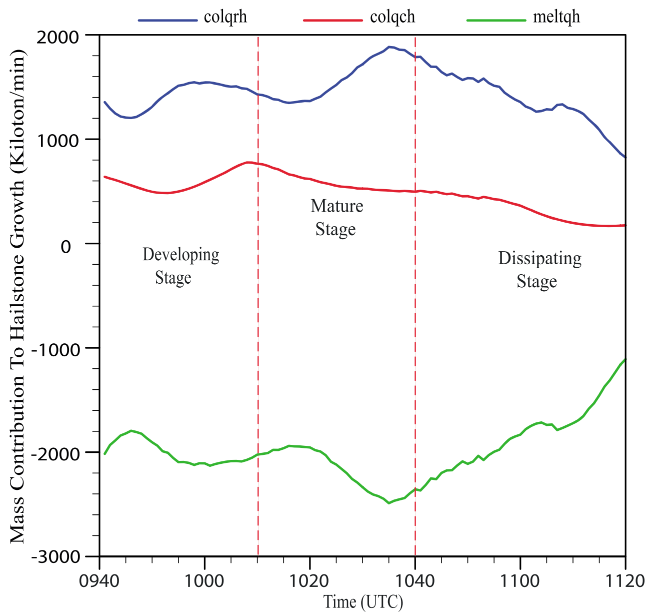

Figure 9. Time series for microphysical budget components in the equation of tendency for hail mass mixing ratio based on the experiment CNTL, during the hailstorm's lifespan. Colored solid lines differentiate the microphysical processes responsible for hailstone growth. As the labels indicate, the microphysical processes include hail collection of rain (colqrh), cloud (colqch), and hail melting to rain (meltqh). Hail mass contributions from other microphysical processes are minimal, which are not shown here.

For the microphysical budget analysis, the components of microphysical processes in the hail mass mixing ratio tendency equation (see MY05b (A7)) are calculated during the storm lifespan (0940 to 1120 UTC), within the domain of Figure 7, extending from the surface to the model top. The dominant processes responsible for hailstone growth are hail collection of rain (colqrh) and of cloud (colqch), and the main hail sink is conversion of hail to rain via melting (meltqh) (Figure 9); contributions from other microphysical processes are minimal and are therefore not shown. Rates of hail collection of rain and cloud water generally increase during the developing stage—hail collection of rain reaches a maximum of about 1900 kt min^{-1} at around 1040 UTC. Between 1020 and 1040 UTC, the dominant sink term, hail melting to rain (negative), also decreases significantly from -2000 to -2600 kt min^{-1} (increases in absolute value), which appears to be associated with more hail falling to the ground and melting during this stage, agreeing with the significant increase in surface hail mass flux from about 0.1×10^7 to 0.8×10^7 kg min^{-1} (Figure 8). It is also noted that the rate of hail collection of cloud water generally decreases from the beginning of the mature stage at 1010 UTC. The reason will be discussed below via more detailed examinations of the microphysical fields. After 1040 UTC, the dominant hail processes, including both sources and sinks, all decrease significantly in magnitude.

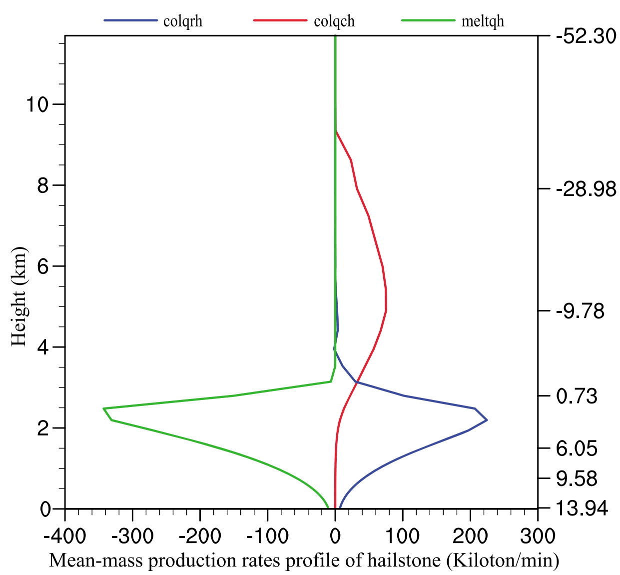

Figure 10. Profiles of the mean mass hail production rates from the processes of hail collection of rain (colqrh), cloud (colqch), and hail melting to rain (meltqh). The profiles are horizontal averages during the hailstorm's life span, between 0940 and 1120 UTC.

The rate profiles of hail collection of rain and cloud, and hail melting to rain, have also been examined based on the microphysical budget of the control simulation. Figure 10 shows the horizontal mean mass hail production rates from the dominant processes between 0940 and 1120 UTC. Results suggest that the process of hail collection of cloud mainly takes place above the freezing level, from 0 to -35°C, with the maximum collection rate at around -10°C (~6 km). While hail collection of rain and hail melting to rain occur in the temperature range of -5°C or higher, with the maximum collection rate at around 0°C (~2.5 km). The larger hail collection rate of rain below the melting level in this study is also consistent with the results of *Heymsfield* [1983]. Based

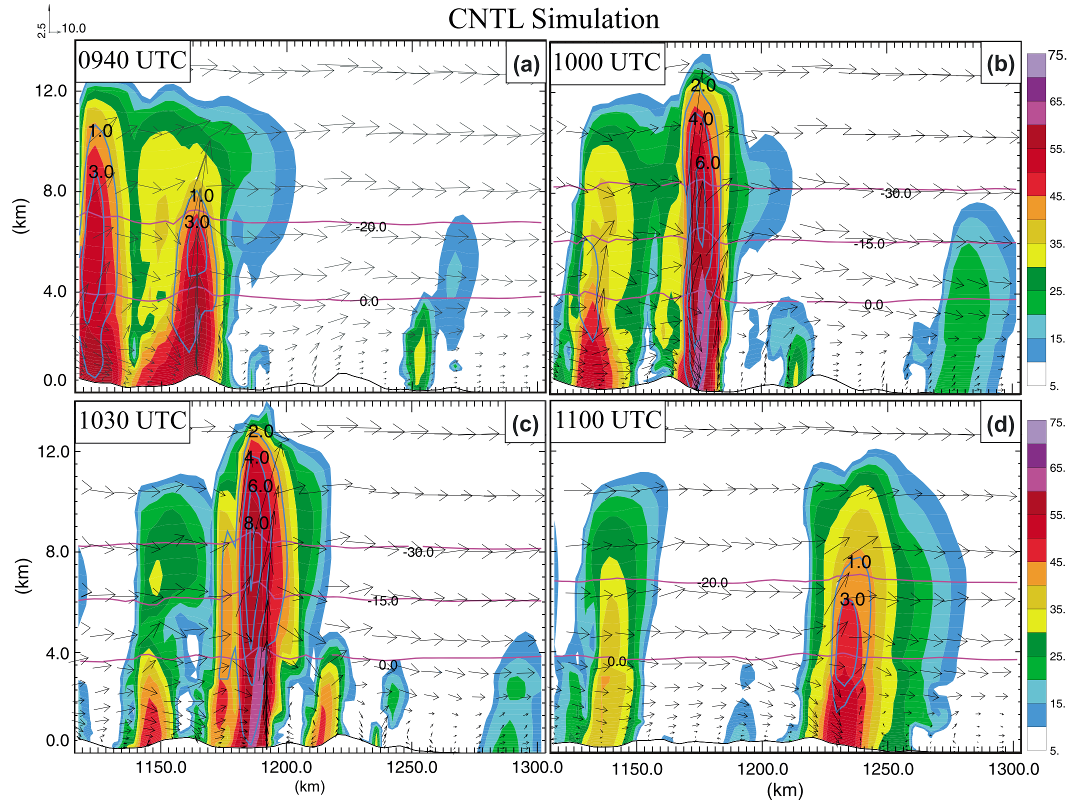

Figure 11. Vertical cross sections of reflectivity (shaded; dBZ), mass content of hail (blue solid contours; g m^{-3}), temperature (purple lines; °C) and u-w wind vectors (arrows) from CNTL during the evolution of the hailstorm at (a) 0940, (b) 1000, (c) 1030, and (d) 1100 UTC on 19 March 2014. Note that at 0940 and 1100 UTC, the contours of temperature (purple lines; °C) are for the −20° and 0°C, while at 1000 and 1030 UTC, they are for −30°, −15°, and 0°C. Horizontal locations of the vertical slices are marked by solid black lines in Figure 7. The locations are shifted slightly to account for storm motion and to cut through the maximum reflectivity core each time.

on the trajectoris calculations of particles from a hailstorm in northeastern Colorado within measured three-dimentational wind field, *Heymsfield* [1983] found that hailstone growth was more rapid after particles became larger during the last few minutes of their growth.

6.2.1. Developing Stage (0940–1010 UTC)

Given the lifecycle of the simulated hailstorm, we will next examine microphysical fields and other related structures in vertical cross sections through the hailstorm. Given the more or less eastward propagation path of the hailstorm, east-west cross sections passing through the primary reflectivity cores (cell B′ in Figure 7) at particular times are chosen. These cross sections shift slightly in the north-south directions, and their locations are indicated by thick straight lines in Figure 7. First, we examine the reflectivity fields and the flow structure of CNTL (Figure 11). Figure 11 shows the hail mass content overlaid with several temperature contours. Figures 12 and 13 contain cross sections of D_m and N_t of hail and rain during the hailstorm evolution. In order to investigate the reason of the reduction of hail collection of cloud since the beginning of the mature stage, Figure 14 presents cross sections of mass content (q) of hail, rain, and cloud at the same locations. These figures are discussed below for each stage of the hailstorm lifecycle.

The reflectivity pattern, as well as the primary circulations of the storm, evolves rapidly during the developing stage. In Figure 11a, the vertical cross section at 0940 UTC shows two storms, with the right storm corresponding to the storm marked as A′ in Figure 7b; this is the main hailstorm. At this time, the reflectivity core (~45 dBZ) appears between 3 and 4 km above the surface, and the maximum updraft speed (at x ~1160 km, z ~6 km) is relatively weak (about 10 m s^{-1}), (Figure 11a). The overlaid hail mass content suggests that during this developing stage, hail mass is mainly concentrated in the layers between 4 and 6 km, within a temperature range of 0° to −20°C. In this region, the mass-weighted mean diameter of hail D_{mh} is generally less than 3 mm, and the total hail number concentration (N_{th}) is over 10^3 m^{-3} (Figure 12a).

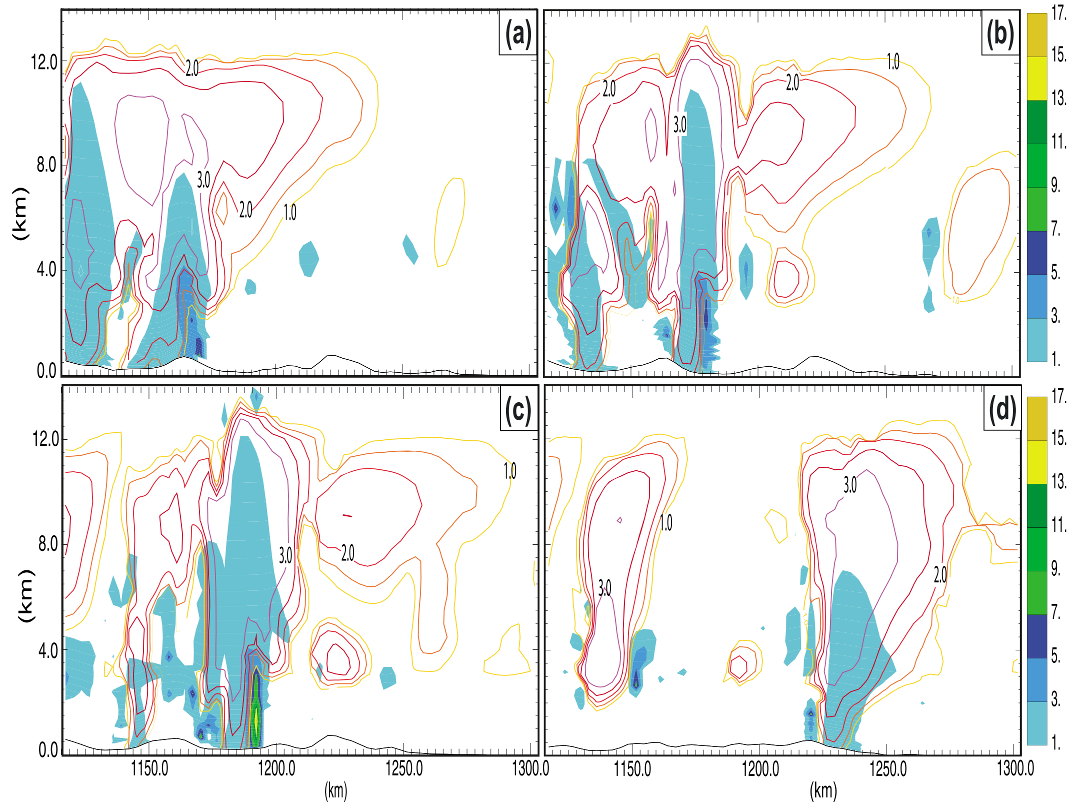

Figure 12. As Figure 11 but for mass-weighted mean diameter (shaded; mm) and total number concentration of hail in base-10 logarithmic scale, i.e., log10(N_{th}) (colored contours; m^{-3}). The contours are from 1.0 to 3.0 at 0.5 intervals.

After about 20 min of development, supported by strong low-level convergence, the updrafts deepen and intensify; the maximum vertical velocity exceeds 20 m s^{-1} at x ~1170 km, z ~6 km. Concurrently, the echo top increases from ~8 to ~12 km, and the reflectivity maximum increases to 65 dBZ (Figure 11b). Reflectivity exceeding 60 dBZ is mostly located below the 0°C temperature level, suggesting that large wet hailstones are presented at lower levels.

Many previous studies have noted that a high concentration of supercooled liquid water in the updraft is required for vigorous hail growth, and in some areas of the storm, they even form accumulation zones [e.g., *Foote*, 1984; *Bringi et al*., 1996; *Kennedy et al*., 2014]. In the initial stage of the storm, large quantities of small rain drops are transported as high as 8 km (x ~1155 km), with N_{tr} = 10–10^3 m^{-3} (Figure 13a). Moreover, this elevated region of supercooled liquid water is maintained throughout the developing and mature stages of the storm, with the region being the deepest during the mature stage, reaching 8 km in altitude (Figure 13b). By 1030 UTC, the top of the region has fallen mostly below 8 km (Figure 13c). Hail number concentration (Figures 12a–12c) is high in regions of supercooled rainwater, agreeing with Figure 9 that accretion of supercooled liquid water within the updraft is a primary hail growth process for this case. The presence of a deep column of supercooled liquid water has been documented in observational studies using polarimetric radar data, indicated by a specific differential phase K_{dp} column. For example, in Fort Collins hailstorms studied by *Kennedy et al*. [2001] K_{dp} columns were as tall as 6 km, K_{dp} is linearly proportional to liquid water content [*Bringi and Chandrasekar*, 2001].

6.2.2. Mature Stage (1010–1040 UTC)

The mature stage of the storm is characterized by a large amount of hailstones falling to the ground, as indicated by the increased surface hail mass flux in Figure 8. During this period, the reflectivity core intensifies and expands and the maximum updraft velocity reaches 22.5 m s^{-1} (Figure 11b). A column of reflectivity exceeding 60 dBZ has descended to the ground by this stage, indicating substantial hailfall at the surface. Rapid descent of the high-reflectivity core has been documented in observed hailstorms [*Heinselman et al*., 2008]. Moreover, the high-reflectivity column seems to shift horizontally from the rear side of the main

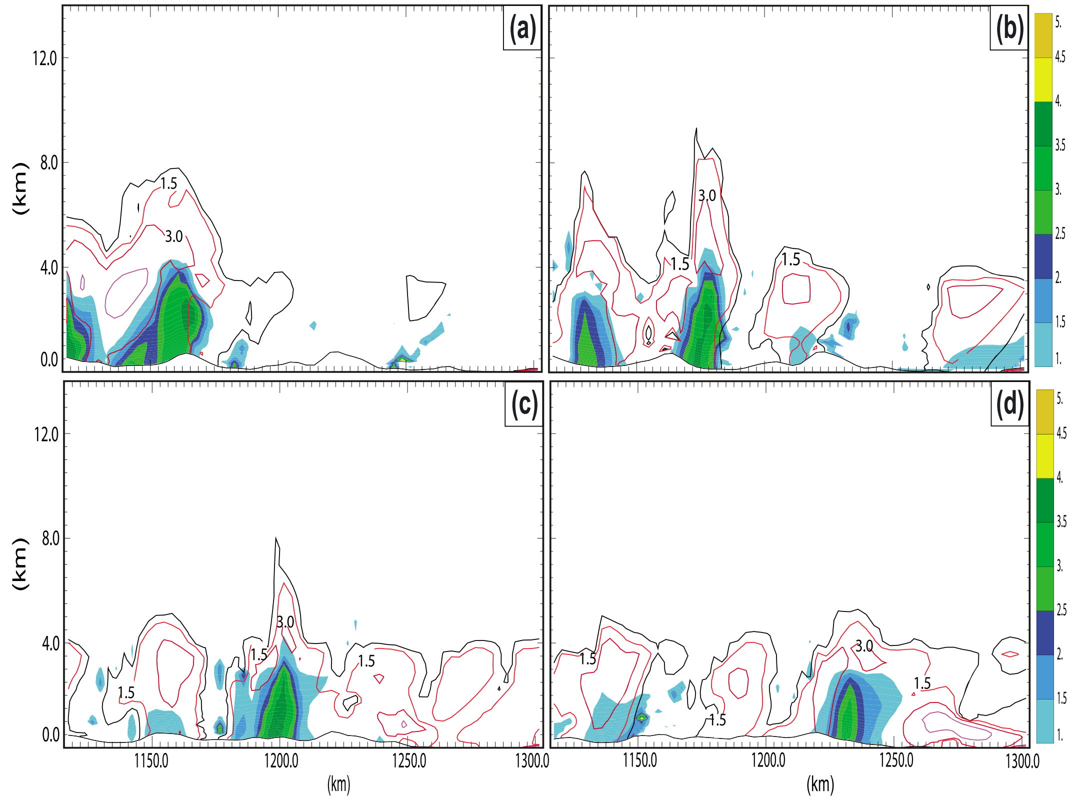

Figure 13. As Figure 12 but for rain only. The contours are from 0.5 to 4.5 at 1.5 intervals.

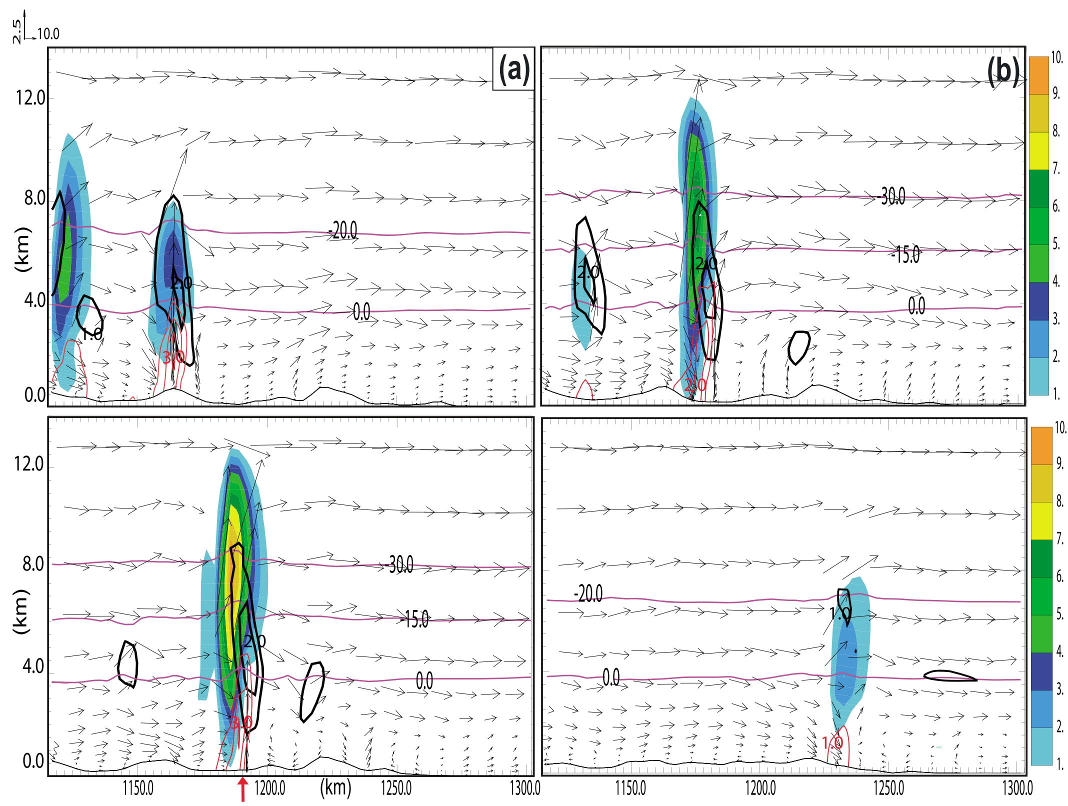

Figure 14. As Figure 11 but for the mass content of hail (shaded; g m^{-3}), rain (red contours; g m^{-3}) and cloud (black contours; g m^{-3}), and wind vectors (arrows). The contour interval of mass content of cloud and rain is 1 g m^{-3}.

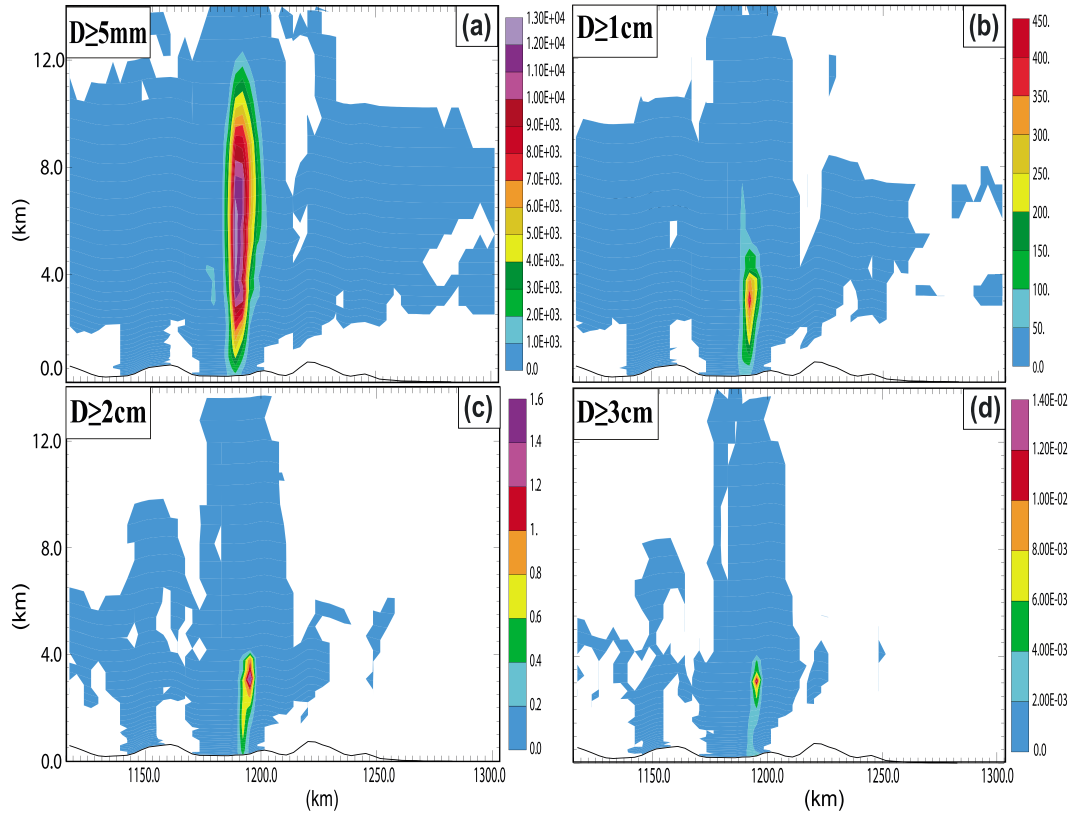

Figure 15. Vertical cross sections of the cumulative total number concentration (m^{-3}) of hail, N_{Dh}, for (a) $D \geq 5$ mm, (b) $D \geq 1$ cm, (c) $D \geq 2$ cm, and (d) $D \geq 3$ cm from the CNTL simulation at 1030 UTC, 19 March 2014 at the same location as in Figure 11c. Note the difference in the color bar for the subpanels.

updrafts (x ~1172 km) at the onset of the mature stage (Figure 11b), to within the updrafts (x ~1194 km) 20 min later (Figure 11c), which seems to be a result of hail size distribution change during this period. Examinations of the corresponding hail size distribution suggest that corresponding to the horizontal shift of the high-reflectivity column, hailstone size increases considerably, especially in the forefront of the storms at the low levels (x ~1190–1195 km, z ~0–2 km), with D_{mh} increasing from ~5 to ~15 mm (Figures 12b and 12c). Large size hailstones in this region conribute considerably to the high reflctivity in this region, leading to the apparent horizontal shift of high-reflectivity column during this stage.

Furthermore, as shown in Figure 14c, during the mature stage, the most hailstone growth occurrs in a region with temperatures between −15° and −30°C (x ~1180−1120 km, z ~5–8 km), which is similar to the hail growth temperature ranges found in observation studies [e.g., *Heymsfield*, 1982, 1983; *Foote*, 1984]. For example, *Heymsfield* [1982] proposed a conceptual model showing hail development over the High Plains, based on radar observaions and calculations of develoment rates of particles into hail within an updraft region. Their conceptual model suggested that ice crystals ascended rapidly to about −25°C after initiation and then descended as they grew within the temperature ranging from −25 to −14°C. It is noted that from 1000 UCT onward, another storm (x ~1126–1141 km) on the left side of the main hailstorm generally dissipates (Figures 14b–14d). Since the microphyical budget analysis is conducted within the domain of Figure 7, the left side storm is also included except the domaint hailstorm. This appears to be the main reason for the decrease in the rate of hail collection of cloud during the mature stage.

The cumulative density function of hail $N_{Dh}(D)$ given by equation (7) is used to identify the concentration of hail larger than a given diameter D during the mature stage. Figure 15 shows the N_{Dh} fields for different D at 1030 UTC using the same vertical cross section as in Figure 11c. Hailstones with $D \geq 5$ mm are concentrated between 2 and 8 km (Figure 15a) above the surface, with reduction in hailstone concentrations below 3 km due to melting. Hailstones with $D \geq 1$ cm are, however, mainly found below 4 km (Figures 15b–15d). This

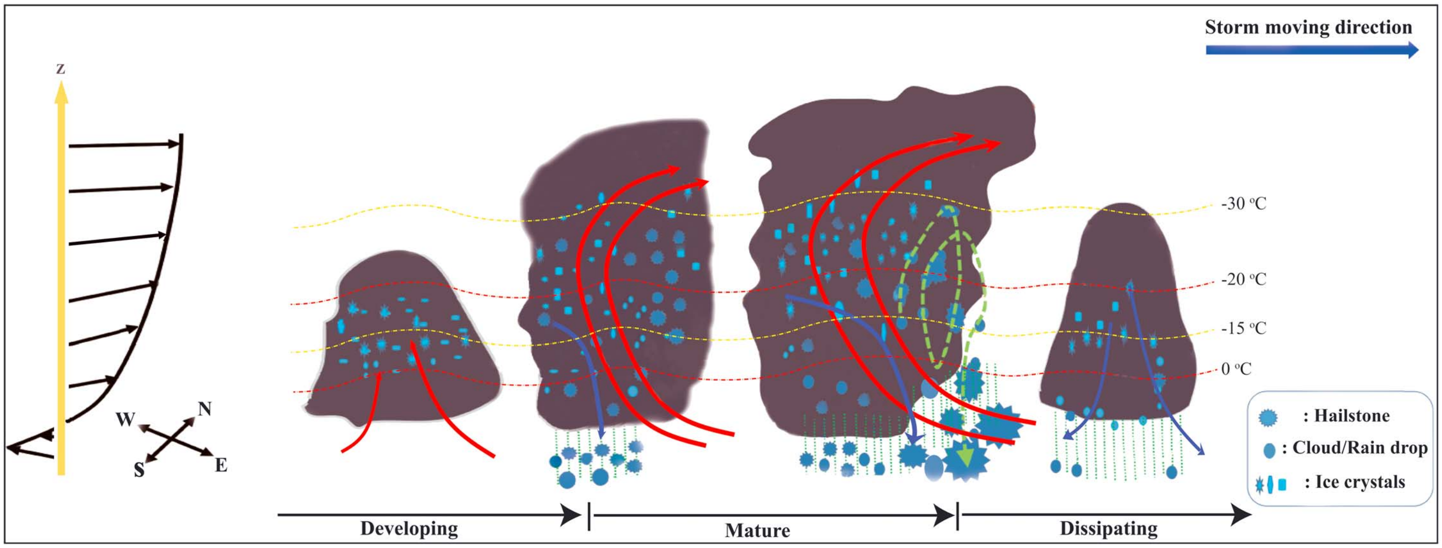

Figure 16. Conceptual model for the evolution of a pulse hailstorm, including the dynamical structure and relevant microphysical processes.

feature of hail size distribution indicates a strong size-sorting effect within the updraft region, which has been highlighted by a number of studies [e.g., *Paluch*, 1978; *Kumjian and Ryzhkov*, 2012; *Dawson et al.*, 2014]. For example, based on idealized simulations of a supercell storm, *Dawson et al.* [2014] found that size sorting of hail posed a dominant impact on simulated differential reflectivity Z_{dr} structures and could also result in a Z_{dr} arc from melting hail even when size sorting was disallowed for raindrops. Nevertheless, the impact of size sorting on the dynamic evolution of storms still remains an open question, and size sorting of hail in pulse-type hailstorms is even less explored. Such effects, while interesting, are beyond the scope of this current paper, however.

6.2.3. Dissipating Stage (1040–1120 UTC)

From 1040 UTC onward, the hailstorm begins to dissipate, indicated by a rapid decrease in surface hail flux (Figure 8). The hailstorm collapses quickly, with the height of the 45 dB*Z* echo top descending from nearly 12 km to about 6 km over a period of 20 min (Figures 11c and 11d). At the same time, the updraft weakens to less than 5 m s^{-1} and the low levels of the storm become dominated by divergent downdrafts exceeding 2 m s^{-1}. The number and size of hailstones arriving at the surface also decrease substantially (Figure 12d).

The rapid dissipation of the hailstorm appeares to be connected with the vertical structure of the storm and the size distribution of falling hailstones, which is strongly affected by size sorting. Given the weak vertical wind shear, the updraft of the storm is relatively upright and lacks the strong rotation present in supercell storms. As such, hailstones and rain drops fall directly down into low-level updrafts (Figure 14c at around x ~1191 km, indicated by a red arrow). Heavy liquid and ice water loading and the associated melting and evaporative cooling are supposed to create large negative buoyancy, turning the updrafts into downdrafts and causing the dissipation of the storm. This is especially true at the leading edge of the storm at the low levels where size sorting leads to the presence of a large number of large hailstones, with $D_{mh} > 17$ mm (Figure 12c, x ~1188 km). We believe the size-sorting effects of falling hydrometeors play active roles in weakening the low-level updrafts and cutting off the low-level inflow, contributing to faster dissipation of the storm. Because of the size-sorting effect, the mean sizes of hydrometeors increase with decreasing height. Larger hailstones tend to fall at higher terminal velocities, they act to weaken the low-level inflow effectively.

6.3. A conceptual Model of the Pulse-Type Hailstorm

Based on CNTL simulation, a schematic conceptual model for the structure and evolution of this particular pulse-type hailstorm and some of its microphysical aspects is proposed in Figure 16.

In the developing stage, aided by large CAPE in the environment, updrafts in the storm rapidly intensify and grow in size and depth. Meanwhile, a large number of small raindrops are transported upward above the freezing level, forming a zone of high supercooled liquid water concentration; such a zone of supercooled liquid water is maintained through most of the developing and mature stages. The deep column of abundant supercooled liquid water plays a significant role for hail mass production, which mainly occurs at temperatures ranging between 0° and −20°C.

The mature stage is characterized by a substantial increase in downward hail flux at the surface. During this stage, updrafts continue to intensify (exceeding 20 m s^{-1}—this value would likely increase further if horizontal grid spacing were reduced), allowing large hailstones to grow in the region with high concentrations of supercooled liquid water. Most hailstone growth happens where temperatures are between −15° and −30°C. A column of high reflectivity at the lower levels descends downward to the ground and also shifts from the rear side of the updrafts to within them. The downward and horizontal shift of the high-reflectivity column appears to be associated with the change of hail size distribution in the storm. During this period, at the leading edge of the storm at the low levels, large hailstones tend to dominate due to the size-sorting effects in the presence of strong low-level inflow [*Dawson et al.*, 2014]. The rapidly falling, large hailstones act to interrupt the updrafts and cut off low-level inflow, resulting in the dissipation of the storm. As a result, the hailstorm is short lived, yielding a pulse-type storm. Hailfall at surface ends abruptly, with strong downdrafts and horizontally divergent flow dominating at low levels. We note that we do not intend to suggest that this proposed conceptual model applies to all pulse-type storms; the generality of the model awaits studies on more of such storms.

7. Summary and Conclusions

This study evaluates the ability of different microphysics schemes within a convective-scale NWP model at 3 km grid spacing to explicitly predict hail in a hailstorm that occurred in Taizhou, Zhejiang province, China on 19 March 2014. The hailstorm environment featured moderately high CAPE of about 2000 J kg^{-1}, while vertical wind shear was mostly unidirectional and confined to the lowest 1.5 km of the atmosphere. Significant low-level convergence was present along an advancing cold front that provided much of the forcing for the hailstorm. The midlevels of the atmosphere were relatively cold and dry. The environment was generally conducive to intense but short-lived hailstorms. Both observed and simulated storms exhibited pulse-type characteristics.

The simulation experiments used one-, two-, and three-moment variants of the Milbrandt and Yau microphysics scheme. Three different two-moment experiments were performed, one which sets the shape parameters of the particle size distributions to zero, one which sets the shape parameter values for rain and hail based on the approximate values of the three-moment simulation, and one which diagnosed the shape parameter of hail as a monotonically increasing function of the hail mean mass-weighted diameter. The simulation results were verified against available observations, namely, the gauge-satellite merged precipitation, radar reflectivity observations (reflectivity and derived maximum estimated size of hail or MESH), and available severe weather reports. The three-moment scheme produced the best simulation in terms of the precipitation distribution and estimated ground-level hail size and amount. The one-moment scheme produced the poorest forecasts.

In terms of the precipitation pattern, the general precipitation systems along the cold frontal zone were reasonably captured in all simulations, except in the simulation using one-moment scheme. For the simulation using one-moment scheme, surface rainfall amount was highly overestimated. Simulations using multimoment schemes produced several small, concentrated areas of high precipitation on the west and northwest side of Taizhou, one of them corresponded to the storm that produced most of the observed hail. The control experiment CNTL, which used the three-moment microphysics scheme, produced a slightly better precipitation pattern than the other experiments.

In terms of the MESH, large differences were noted among the simulations. Experiment CNTL produced maximum values of MESH of more than 40 mm, similar to radar-derived MESH values, while the one-moment scheme and variants of two-moment schemes produced maximum values of no more than 30 mm. The MESH swath of CNTL also exhibited an east-west orientation, consistent with the eastward movement of the observed hailstorm. The primary discrepancy between CNTL-simulated MESH and radar-derived MESH was a displacement of the simulated MESH field of around 60 km to the west. The simulated hailstorm was also delayed by about 1 h, compared to observations. Considering the over 20 h of lead time of the simulation, such spatial and temporal errors are considered reasonable, and such forecasts would certainly be of value to operational forecasters.

This paper further investigated the microphysical characteristics of the simulated hailstorm during its life cycle using CNTL, which produced the most accurate forecast. According to the time series of surface hail mass flux, the life cycle of the hailstorm is divided into three stages: the developing stage, the mature stage, and the dissipating stage. In the developing stage, hardly any hail reached the ground, while peak surface hail flux was reached in the mature stage. In the dissipating stage, surface hail flux was still significant but decreased rapidly. A microphysical budget analysis based on the tendency of hail mass mixing ration of the experiment CNTL was also performed. Results suggested that the dominant processes responsible for hailstone growth were hail collection of rain and cloud water, and the main sink of hail was conversion of hail to rain via melting. Contributions from other microphysical processes were negligibly small. The contribution rates of dominant responsible microphysical processes, i.e., hail collection of rain and melting of hail, generally increased in magnitude during the developing and mature stages and decreased in magnitude during the dissipating stage. The hail production rate profiles from the dominant microphysical processes suggest that the process of hail collection of cloud mainly takes place above the freezing level, with the maximum collection rate at around $-10°C$, while the processes of hail collection of rain and hail melting to rain occur in the temperature range of $-5°C$ or higher, with the maximum collection rate at around 0°C.

For different stages of the hailstorm development, the simulated reflectivity, mass content, total number concentration, accumulative hail number above certain size thresholds, and mean mass diameter of hail were examined. The rainwater mass content and number concentration were also examined. Based on examinations of the dynamic and microphysical structures and the evolution characteristics during the storm's short lifespan, a conceptual model for this pulse-type hailstorm is proposed.

The results of this study suggest that multimoment microphysics schemes are most useful in predicting the size and quantities of hail, which is consistent with other studies using multimoment schemes [*Milbrandt and Yau*, 2006b; *Thompson et al*., 2008; *Loftus and Cotton*, 2014]. While the results are encouraging, these findings and the conceptual model are based on a single case only. For more general applicability, more case studies or statistical studies are needed. This study is also limited by the lack of in situ microphysical observations as well as quantitative surface hail observations. For more reliable verification of the microphysical characteristics in the simulated hailstorm, direct observations of microphysical processes are needed. More quantitative diagnostics of the microphysical processes within the model would also be beneficial. We plan to perform more detailed diagnostics in the future. This study represents one of few case studies using real data that attempt to perform direct prediction of hailstones, to evaluate the prediction against available data, and to understand the microphysics within the constraints of limited in situ microphysical observations. For future studies, we will also attempt to use higher spatial resolutions to hopefully more accurately reproduce observed hailstorms and associated hailfall.

Acknowledgments
This work was primarily supported by the Ministry of Science and Technology of the People's Republic of China (MOST) (2013CB430103) and the National Science Foundation of China (41405100). This work is also supported by the Foundation of China Meteorological Administration special (GYHY201506006). Liping Luo was supported by Nanjing University for her extended visit at the Center for Analysis and Prediction of Storms, University of Oklahoma. We gratefully acknowledge the High Performance Center (HPCC) of Nanjing University for doing the numerical calculations in this paper on its IBM Blade cluster system. The second author acknowledges the support of the National Thousand Person Plan hosted at the Nanjing University and the support of NSF grants AGS-1261776 for the Severe Hail, Analysis, Representation, and Prediction (SHARP) project. Nathan Snook and Jonathan Labriola are thanked for proofreading and improving the manuscript. Suggestions and comments from three anonymous reviewers also improved our paper. The NCEP FNL analysis data can be downloaded freely at http://rda.ucar.edu/datasets/ds083.2/, and the 0.5°×0.5° real-time analysis data can be downloaded freely at https://www.ncdc.noaa.gov/data-access/model-data/model-datasets/global-forcast-system-gfs. The CMORPH precipitation data can be downloaded freely at http://data.cma.cn/data/detail/dataCode/SEVP_CLI_CHN_MERGE_CMP_PRE_HOUR_GRID_0.10/keywords/cmorph.html. The ARPS model code is available from CAPS, University of Oklahoma, 100 E Boyd St, Norman OK 73019, at http://arps.caps.ou.edu/arpsdown.html. The radar observation is provided by the Climatic Data Center at National Meteorological Information Center of China Meteorological Administration, available at https://pan.baidu.com/s/1jHMvEBk (password: c2sq).

References

Adams-Selin, R. D., and C. L. Ziegler (2016), Forecasting hail using a one-dimensional hail growth model within WRF, *Mon. Weather Rev.*, *144*(12), 4919–4939.

Brimelow, J. C., and G. W. Reuter (2009), Explicit forecasts of hail occurrence and expected hail size using the GEM–HAILCAST system with a rainfall filter, *Weather Forecast.*, *24*(4), 935–945.

Brimelow, J. C., G. W. Reuter, and E. R. Poolman (2002), Modeling maximum hail size in Alberta thunderstorms, *Weather Forecast.*, *17*(5), 1048–1062.

Bringi, V. N., and V. Chandrasekar (2001), *Polarimetric Doppler Weather Radar*, pp. 159–160, Cambridge Univ. Press, Cambridge.

Bringi, V. N., L. Liu, P. C. Kennedy, and V. Chandrasekar (1996), Dual multiparameter radar observations of intense convective storms: The 24 June 1992 case study, *Meteorog. Atmos. Phys.*, *59*(1), 3–31.

Bryan, G. H., and H. Morrison (2012), Sensitivity of a simulated squall line to horizontal resolution and parameterization of microphysics, *Mon. Weather Rev.*, *140*(1), 202–225.

Burgess, D. W, and L. R. Lemon (1990), *Severe Thunderstorm Detection by Radar*, pp. 619–647, Radar in Meteorol., Springer, Boston, Mass.

Cerniglia, C. S., and W. R. Snyder (2002), Development of warning criteria for severe pulse thunderstorms in the northeastern United States using the WSR-88D, *Eastern Region Tech. Attachment*, *3*, 14.

Cheng, L., and M. English (1982), A relationship between hailstone concentration and size, *J. Atmos. Sci.*, *40*(1), 204–213.

Costa, S., P. Mezzasalma, V. Levizzani, P. P. Alberoni, and S. Nanni (2001), Deep convection over northern Italy: Synoptic and thermodynamic analysis, *Atmos. Res.*, *56*(1), 73–88.

Craven, J. P., H. E. Brooks, J. A. Hart, and A. M. S. Ams (2004), Baseline Climatology of Sounding Derived Parameters Associated With Deep, Moist Convection, *Natl. Wea. Dig.*, *28*(1), 13–24.

Dawson, D. T., M. Xue, J. A. Milbrandt, and M. Yau (2010), Comparison of evaporation and cold pool development between single-moment and multimoment bulk microphysics schemes in idealized simulations of tornadic thunderstorms, *Mon. Weather Rev.*, *138*(4), 1152–1171.

Dawson, D. T., M. Xue, J. A. Milbrandt, and A. Shapiro (2015), Sensitivity of real-data simulations of the 3 May 1999 Oklahoma City tornadic supercell and associated tornadoes to multimoment microphysics. Part I: Storm- and tornado-scale numerical forecasts, *Mon. Weather Rev.*, *143*(6), 2241–2265.

Dawson, D. T., E. R. Mansell, Y. Jung, L. J. Wicker, M. R. Kumjian, and M. Xue (2014), Low-level Z DR signatures in supercell forward flanks: The role of size sorting and melting of hail, *J. Atmos. Sci.*, *71*(1), 276–299.

Ding, Y. (1994), Monsoons over China, *Adv. Atmos. Sci.*, *11*(2), 252–252.

Fan, J., L. R. Leung, Z. Li, H. Morrison, H. Chen, Y. Zhou, Y. Qian, and Y. Wang (2012), Aerosol impacts on clouds and precipitation in eastern China: Results from bin and bulk microphysics, *J. Geophys. Res.*, *117*, D00K36, doi:10.1029/2011JD016537.

Fernández-González, S., P. K. Wang, E. Gascón, F. Valero, and J. L. Sánchez (2016), Latent cooling and microphysics effects in deep convection, *Atmos. Res.*, *180*, 189–199.

Foote, G. B. (1984), A study of hail growth utilizing observed storm conditions, *J. Clim. Appl. Meteorol.*, *23*(1), 84–101.

Gagne, I. I. D. J, McGovern, A., Ming X (2014), Machine learning enhancement of storm scale ensemble precipitation forecasts, *Weather Forecast.*, *29*(4), 1024–1043.

García-Ortega, E., A. Merino, L. López, and J. L. Sánchez (2012), Role of mesoscale factors at the onset of deep convection on hailstorm days and their relation to the synoptic patterns, *Atmos. Res. 114–115*(4), 91–106.

García-Ortega, E., J. Lorenzana, A. Merino, S. Fernández-González, L. López, and J. L. Sánchez (2017), Performance of multi-physics ensembles in convective precipitation events over northeastern Spain, *Atmos. Res.*, *190*, 55–67.

Guo, X., and M. Huang (2002), Hail formation and growth in a 3D cloud model with hail-bin microphysics, *Atmos. Res.*, *63*(1–2), 59–99.

Heinselman, P. L., D. L. Priegnitz, K. L. Manross, T. M. Smith, and R. W. Adams (2008), Rapid sampling of severe storms by the national weather radar testbed phased array radar, *Weather Forecast.*, *23*(5), 808–824.

Heymsfield, A. J. (1982), A comparative study of the rates of development of potential graupel and hail embryos in high plains storms, *J. Atmos. Sci.*, *39*(12), 2867–2897.

Heymsfield, A. J. (1983), Case study of a hailstorm in Colorado. Part IV: Graupel and hail growth mechanisms deduced through particle trajectory calculations, *J. Atmos. Sci.*, *40*(6), 1482–1509.

Joyce, R. J., J. E. Janowiak, P. A. Arkin, and P. Xie (2004), CMORPH: A method that produces global precipitation estimates from passive microwave and infrared data at high spatial and temporal resolution. *J. Hydrometeorol.*, *5*, 487–503.

Kennedy, P. C., S. A. Rutledge, W. A. Petersen, and V. N. Bringi (2001), Polarimetric radar observations of hail formation, *J. Appl. Meteorol.*, *40*(8), 1347–1366.

Kennedy, P. C., S. A. Rutledge, B. Dolan, and E. Thaler (2014), Observations of the 14 July 2011 Fort Collins hailstorm: Implications for WSR-88D-based hail detection and warnings, *Weather Forecast.*, *29*(3), 623–638.

Khain, A., M. Ovtchinnikov, M. Pinsky, A. Pokrovsky, and H. Krugliak (2000), Notes on the state-of-the-art numerical modeling of cloud microphysics, *Atmos. Res.*, *55*(3–4), 159–224.

Khain, A., A. Pokrovsky, M. Pinsky, A. Seifert, and V. Phillips (2004), Simulation of effects of atmospheric aerosols on deep turbulent convective clouds using a spectral microphysics mixed-phase cumulus cloud model. Part I: Model description and possible applications, *J. Atmos. Sci.*, *61*(24), 2963–2982.

Khain, A., K. Beheng, A. Heymsfield, A. Korolev, S. Krichak, Z. Levin, M. Pinsky, V. Phillips, T. Prabhakaran, and A. Teller (2015), Representation of microphysical processes in cloud-resolving models: Spectral (bin) microphysics versus bulk parameterization, *Rev. Geophys.*, *53*, 247–322, doi:10.1002/2014RG000468.

Khain, A. P., and I. Sednev (1996), Simulation of precipitation formation in the Eastern Mediterranean coastal zone using a spectral microphysics cloud ensemble model, *Atmos. Res.*, *43*, 77–110.

Knight, C. A., and N. C. Knight (2001), Hailstorms, in *Severe Convective Storms*, edited by C. A. Doswell, III, pp. 223–254, Am. Meteorol. Soc., Boston, Mass.

Kumjian, M. R., and A. V. Ryzhkov (2012), The impact of size sorting on the polarimetric radar variables, *J. Atmos. Sci.*, *69*(6), 2042–2060.

Li, X., W.-K. Tao, A. P. Khain, J. Simpson, and D. E. Johnson (2009), Sensitivity of a cloud-resolving model to bulk and explicit bin microphysical schemes. Part I: Comparisons, *J. Atmos. Sci.*, *66*(1), 3–21.

Lynn, B. H., A. P. Khain, J. Dudhia, D. Rosenfeld, A. Pokrovsky, and A. Seifert (2005a), Spectral (bin) microphysics coupled with a mesoscale model (MM5). Part II: Simulation of a CaPE rain event with a squall line, *Mon. Weather Rev.*, *133*(1), 59–71.

Lynn, B. H., A. P. Khain, J. Dudhia, D. Rosenfeld, A. Pokrovsky, and A. Seifert (2005b), Spectral (bin) microphysics coupled with a mesoscale model (MM5). Part I: Model description and first results, *Mon. Weather Rev.*, *133*(1), 44–58.

Loftus, A., and W. Cotton (2014), A triple-moment hail bulk microphysics scheme. Part II: Verification and comparison with two-moment bulk microphysics, *Atmos. Res.*, *150*, 97–128.

Milbrandt, J., and M. Yau (2005a), A multimoment bulk microphysics parameterization. Part II: A proposed three-moment closure and scheme description, *J. Atmos. Sci.*, *62*(9), 3065–3081.

Milbrandt, J., and M. Yau (2005b), A multimoment bulk microphysics parameterization. Part I: Analysis of the role of the spectral shape parameter, *J. Atmos. Sci.*, *62*(9), 3051–3064.

Milbrandt, J., and M. Yau (2006a), A multimoment bulk microphysics parameterization. Part III: Control simulation of a hailstorm, *J. Atmos. Sci.*, *63*(12), 3114–3136.

Milbrandt, J., and M. Yau (2006b), A multimoment bulk microphysics parameterization. Part IV: Sensitivity experiments, *J. Atmos. Sci.*, *63*(12), 3137–3159.

Morrison, H., G. Thompson, and V. Tatarskii (2009), Impact of cloud microphysics on the development of trailing stratiform precipitation in a simulated squall line: Comparison of one- and two-moment schemes, *Mon. Weather Rev.*, *137*(3), 991–1007.

Moore, J. T., and J. P. Pino (1990), An interactive method for estimating maximum hailstone size from forecast soundings, *Weather Forecast.*, *5*(3), 508–525.

Paluch, I. R. (1978), Size sorting of hail in a three-dimensional updraft and implications for hail suppression, *J. Appl. Meteorol.*, *17*(6), 763–777.

Shen, Y., P. Zhao, Y. Pan, and J. Yu (2014), A high spatiotemporal gauge-satellite merged precipitation analysis over China, *J. Geophys. Res. Atmos.*, *119*, 3063–3075, doi:10.1002/2013JD020686.

Snook, N., Y. Jung, J. Brotzge, B. Putnam, and M. Xue (2016), Prediction and ensemble forecast verification of hail in the supercell storms of 20 May 2013, *Weather Forecast.*, *31*(3), 811–825.

Sun WY, and Chang CZ (1986), Diffusion model for a convective layer. Part I: Numerical simulation of convective boundary layer, *J. Appl. Meteorol.*, *25*(10), 1445–1453.

Thompson, G., P. R. Field, R. M. Rasmussen, and W. D. Hall (2008), Explicit forecasts of winter precipitation using an improved bulk microphysics scheme. Part II: Implementation of a new snow parameterization, *Mon. Weather Rev.*, *136*(12), 5095–5115.

Webb, J. D., and R. Muirhead (2002), Severe hailstorm over west Cornwall on 25 August 2000, *Weather*, *57*(10), 371–374.
Witt, A., M. D. Eilts, G. J. Stumpf, J. Johnson, E. D. W. Mitchell, and K. W. Thomas (1998), An enhanced hail detection algorithm for the WSR-88D, *Weather Forecast.*, *13*(2), 286–303.
Xue, M., K. Droegemeier, V. Wong, A. Shapiro, and K. Brewster (1995), ARPS version 4.0 user's guide, *Center for Analysis and Prediction of Storms, University of Oklahoma*, 380 pp. [Available at http://www.caps.ou.edu/ARPS.]
Xue, M., K. K. Droegemeier, and V. Wong (2000), The Advanced Regional Prediction System (ARPS)—A multi-scale nonhydrostatic atmospheric simulation and prediction model. Part I: Model dynamics and verification, *Meteorog. Atmos. Phys.*, *75*(3–4), 161–193.
Xue, M., K. K. Droegemeier, V. Wong, A. Shapiro, K. Brewster, F. Carr, D. Weber, Y. Liu, and D. Wang (2001), The Advanced Regional Prediction System (ARPS)—A multi-scale nonhydrostatic atmospheric simulation and prediction tool. Part II: Model physics and applications, *Meteorog. Atmos. Phys.*, *76*(3–4), 143–165.
Xue, M., D. Wang, J. Gao, K. Brewster, and K. K. Droegemeier (2003), The Advanced Regional Prediction System (ARPS), storm-scale numerical weather prediction and data assimilation, *Meteorog. Atmos. Phys.*, *82*(1), 139–170.
Zalesaka, S. T. (1979), Fully multidimensional flux-corrected transport algorithms for fluids, *J. Comput. Phys.*, *31*(3), 335–362.
Zhang, C., Q. Zhang, and Y. Wang (2008), Climatology of hail in China: 1961–2005, *J. Appl. Meteorol. Climatol.*, *47*(3), 795–804.